Performance improvement of ballasted railway tracks using three-dimensional cellular geoinclusions

Piyush Punetha[a] and Sanjay Nimbalkar[b]✉

[a] PhD Candidate, School of Civil and Environmental Engineering, University of Technology Sydney, 15 Broadway, Ultimo NSW–2007, Australia. Email address: Piyush.Punetha@student.uts.edu.au

[b] Senior Lecturer, School of Civil and Environmental Engineering, University of Technology Sydney, 15 Broadway, Ultimo NSW–2007, Australia. Email address: Sanjay.Nimbalkar@uts.edu.au

✉ Corresponding author: Dr Sanjay Nimbalkar, Senior Lecturer, School of Civil and Environmental Engineering, University of Technology Sydney, 15 Broadway, Ultimo NSW–2007, Australia. Email address: Sanjay.Nimbalkar@uts.edu.au. Telephone no.: +61 2 9514 1819

Number of words (main text): 6760
Number of figures: 16
Number of tables: 5

ABSTRACT

Three-dimensional (3D) cellular inclusions such as geocells and scrap rubber tyres improve the engineering properties of the infill materials by providing all-around confinement. Although the 3D geoinclusions possess immense potential in the railway industry, their application is still limited due to a lack of adequate techniques to evaluate the magnitude of improvement provided by these artificial inclusions. This article presents an innovative computational approach to evaluate the effectiveness of 3D cellular geoinclusions in improving the performance of ballasted railway tracks. The proposed method is an integrated approach that combines the additional confinement model with the geotechnical rheological model for a railway track. The methodology is applied to an open track-bridge transition, and the results revealed that the geoinclusions substantially reduce the differential settlement. However, the magnitude of improvement depends on the opening size, placement location within the track and material used to manufacture the cellular inclusions. Moreover, the magnitude of settlement reduction also depends on the axle load and subgrade soil properties. The proposed methodology can assist the railway engineers in assessing the efficacy of 3D inclusions in improving the performance of railway tracks and help select the most appropriate material, size, and location of reinforcement for deriving maximum benefits.

Keywords: Geosynthetics; Cellular geoinclusions; Railway tracks; Rheological model; Settlement; Transition zone

1. Introduction

The conventional ballasted railway tracks rely on several granular layers such as ballast, subballast and fill, to safely transmit the train-induced loads to the subgrade soil. These granular layers undergo resilient and inelastic (plastic) deformations under repetitive train loading (Selig and Waters, 1994). The differential settlement produced due to uneven plastic deformation in these layers adversely affects the track stability and demands frequent maintenance operations to restore the track geometry (Esveld, 2001). A rapid hike in the axle loads and traffic volume over the last few decades has accelerated the deformation in the track layers and incurred significant maintenance costs (Nimbalkar and Indraratna, 2016; Punetha et al., 2020a).

The differential settlement problem is even more severe for the critical zones along railway lines, such as transitions between standard track and bridge, tunnel, underpass or culvert. These regions are highly susceptible to swift degradation in track geometry due to inhomogeneous support conditions along the track length. Although significant advances have been achieved in the past to mitigate this problem, it remains a subject of concern, as evidenced by the poor performance of transition zones at several locations (Wang et al., 2018).

The inadequate confinement of the granular layers is one of the primary reasons for the track geometry degradation (Li et al., 2016; Nimbalkar et al., 2020). The 3D cellular geoinclusions, such as geocells or scrap rubber tyres, may prove highly beneficial in this aspect as they can enhance the strength and stiffness of the granular layers by providing extra confinement (Avesani Neto, 2019; Cowland and Wong, 1993; Garga and O'Shaughnessy, 2000; Inti and Tandon, 2021; Leshchinsky and Ling, 2013a; Pokharel et al., 2010; Rajagopal et al., 1999; Song et al., 2019). The geocells are made up of thin polymeric strips [most commonly high-density polyethylene (HDPE)] that are welded or bonded along their width at regular intervals to form a 3D cellular network. They can also be manufactured using a variety of other materials such as geogrids, geotextiles, geonets, bamboo and rubber (Punetha et al., 2020b). They are usually shipped to the project site in a collapsed configuration and subsequently expanded like an accordion and filled with soil. Similar to geocells, scrap rubber tyres (after removing one sidewall) can be arranged on the site to form a 3D cellular network and then filled with the granular material. Geoinclusions can be incorporated into the ballast, subballast or top of the subgrade layer of a ballasted railway track. The most appropriate placement location for geoinclusions is typically governed by the properties of subgrade soil, geoinclusion material and the intended function of geoinclusions (i.e., to reduce subgrade stress or the lateral deformation of ballast and subballast layers, or both) (Nimbalkar et al., 2020).

The application of 3D cellular geoinclusions can be highly beneficial for the long-term stability of ballasted railway tracks. These inclusions can help to reduce the lateral and vertical deformations of the track layers, thereby preserving the track geometry (Chrismer, 1997). They increase the stiffness of infill material, which can aid in the uniform distribution of the traffic-induced stresses over a wide area of subgrade (Zhou and Wen, 2008). They can also alleviate or redistribute the shear stresses at the ballast-subballast or subballast-subgrade interface, depending on the placement location (Giroud and Han, 2004). Previous field investigations have also shown that the use of cellular geoinclusions in the ballasted railway track: (a) significantly reduces the settlement and lateral deformations (Raymond, 2001); (b) curtails the magnitude of stress transmitted to the subgrade soil (Zarembski et al., 2017); and (c) increases the track stiffness and reduces the rate of track geometry degradation (Kaewunruen et al., 2016).

It should be emphasised that the performance of the geoinclusion reinforced layer depends on several aspects, including properties of inclusion, infill soil and subgrade, loading conditions, and placement position. A detailed analysis of these factors is imperative before placing geoinclusion in the track. Nevertheless, the cellular geoinclusions may lose their ability to confine the infill soil if their structural integrity is compromised by rupture of joints (bonds or seams) under high service loads or by wear and tear during the installation (Yang et al., 2013). This important aspect must be considered while selecting the type of inclusion for railway application.

Figure 1 illustrates the differential settlement problem encountered in a typical open track-bridge transition without any countermeasure. As can be seen, the track supported by soil layers (softer side) settles more than that founded on the bridge (stiffer side) after several load repetitions. The 3D cellular geoinclusions can reduce the plastic deformation in the granular layers by providing additional confinement. Consequently, employing these inclusions to strengthen the softer side of the critical zone may reduce the uneven track displacement and improve their performance in a cost-effective manner.

Despite the immense potential, the application of 3D artificial inclusions in railway tracks is still minimal due to the lack of a well-established method to evaluate the magnitude of improvement provided by these geoinclusions. To tackle this issue, some researchers have resorted to finite element (FE) analyses to explore the beneficial aspects of geoinclusions in improving track performance (e.g., Banerjee et al., 2020a; Leshchinsky and Ling, 2013b). A few researchers also investigated the effectiveness of geoinclusions in railway tracks using discrete element (DE) analyses (Chen et al., 2012; Liu et al., 2018, 2020). In these analyses, the geoinclusion and infill materials were simulated as a layer of spheres and clumps/clusters (a group of spheres that are bonded together), respectively. The main advantage of using DE method over continuum-based FE approaches is that it can accurately capture the behaviour of distinct infill particles and simulate the particle motion. On the other hand, FE approach can handle the layered track substructure, constitutive relationships, interface behaviour and long-term track response. However, the FE and DE methods are computationally intensive and may require a relatively large amount of time to accurately predict the track response, especially when the number of load repetitions or train passages is huge. The analytical approaches offer comparatively faster and computationally more efficient alternatives to DE or FE analyses for evaluating the performance of reinforced railway tracks; however, such methods are relatively scarce.

In view of the above discussion, this study provides a novel computational methodology that incorporates the effect of geoinclusion on the behaviour of a ballasted railway track. The proposed method is an integrated approach that combines the additional confinement model with the geotechnical rheological model for a railway track. The accuracy of the approach is verified by comparing the predicted results against the data reported in the literature. The proposed methodology is applied to an open track-bridge transition to demonstrate its practical applicability, and the adequacy of artificial inclusions in mitigating the differential settlements is investigated. Finally, a parametric study is conducted to assess the influence of factors such as axle load, subgrade properties, placement location, type, and opening size of geoinclusion on the track settlement. The key novelty of this work is the development of an analytical framework to investigate the effect of 3D cellular geoinclusions on the behaviour of ballasted railway tracks, especially at a transition zone. This study provides a computational tool that the practising railway engineers can use to improve the performance of the ballasted railway tracks, especially in the transition zones.

2. Methodology

The proposed computational method is an integrated approach that combines the geotechnical rheological track model and additional confinement model to predict the response of railway tracks reinforced with 3D cellular inclusions.

2.1. Rheological track model

A geotechnical rheological model is utilised to predict the response of a railway track under train-induced repeated loading (Punetha et al., 2021). Figure 2 shows the simplified geotechnical rheological model of a ballasted railway track considered in this study. The track substructure in this model comprises three geotechnical layers: ballast, subballast and subgrade. These layers are represented as an array of lumped masses connected with elastic springs, viscous dashpots, and plastic slider elements. The springs and dashpots reproduce the viscoelastic behaviour, whereas the slider elements simulate the inelastic response of the track layers. Thus, the total response of the substructure layers can be represented as the sum of viscoelastic and plastic components:

$$\mathrm{d}w(t) = \mathrm{d}w^{ve}(t) + \mathrm{d}w^{p}(t) \tag{1}$$

where *dw* denotes the vertical displacement increment (m); superscripts *ve* and *p* stand for the viscoelastic and plastic parts of the response, respectively. It must be noted that the dashpot represents the material damping or the dissipation of elastic energy by the material during train-induced repeated loading. The granular materials usually dissipate this energy hysteretically, by the slippage of particles against each other (Kramer, 1996).

The magnitude of the plastic part in Equation (1) depends on the state of the slider element. If the slider element is active, the total response of a substructure layer is essentially viscoelastic-plastic [$dw^p(t) \neq 0$], whereas the viscoelastic behaviour is reproduced if this element is inactive [$dw^p(t) = 0$]. The activation or deactivation of this element depends on its yield criterion (*f*) and is governed by the loading-unloading conditions or Kuhn-Tucker relations (Simo and Hughes, 1998). Accordingly, the slider element remains in the active state as long as the yield criterion is met and remains satisfied. The magnitude of movement incurred in a slider element during the activated phase (dw^p) is determined using appropriate constitutive relationships, as discussed later in Section 2.1.2.

2.1.1. Equation of motion

The total response of the track substructure layers under train-induced loading is determined by utilising the following equation of motion, which is derived by applying the dynamic equilibrium condition in Figure 2:

$$\begin{aligned}\boldsymbol{M}d\ddot{\boldsymbol{w}}_{\mathbf{m}} + \boldsymbol{C}d\dot{\boldsymbol{w}}_{\mathbf{m}} + \boldsymbol{K}d\boldsymbol{w}_{\mathbf{m}} - \boldsymbol{C}^{\boldsymbol{p}}d\dot{\boldsymbol{w}}^{\boldsymbol{p}}_{\mathbf{m}} - \boldsymbol{K}^{\boldsymbol{p}}d\boldsymbol{w}^{\boldsymbol{p}}_{\mathbf{m}} - \boldsymbol{C}'\{d\dot{\boldsymbol{w}}_{\mathbf{m-1}} + d\dot{\boldsymbol{w}}_{\mathbf{m+1}}\} - \boldsymbol{K}'\{d\boldsymbol{w}_{\mathbf{m-1}} + d\boldsymbol{w}_{\mathbf{m+1}}\} \\ + \boldsymbol{C}^{\boldsymbol{p}'}\{d\dot{\boldsymbol{w}}^{\boldsymbol{p}}_{\mathbf{m-1}} + d\dot{\boldsymbol{w}}^{\boldsymbol{p}}_{\mathbf{m+1}}\} + \boldsymbol{K}^{\boldsymbol{p}'}\{d\boldsymbol{w}^{\boldsymbol{p}}_{\mathbf{m-1}} + d\boldsymbol{w}^{\boldsymbol{p}}_{\mathbf{m+1}}\} = d\boldsymbol{F}\end{aligned} \qquad (2)$$

where,

$$\boldsymbol{M} = \begin{bmatrix} m_{\mathrm{g}} & 0 & 0 \\ 0 & m_{\mathrm{s}} & 0 \\ 0 & 0 & m_{\mathrm{b}} \end{bmatrix}; \boldsymbol{C} = \begin{bmatrix} c_{\mathrm{g}} + c_{\mathrm{s}} + 2c^{s}_{\mathrm{g}} & -c_{\mathrm{s}} & 0 \\ -c_{\mathrm{s}} & c_{\mathrm{s}} + c_{\mathrm{b}} + 2c^{s}_{\mathrm{s}} & -c_{\mathrm{b}} \\ 0 & -c_{\mathrm{b}} & c_{\mathrm{b}} + 2c^{s}_{\mathrm{b}} \end{bmatrix}; \boldsymbol{K} = \begin{bmatrix} k_{\mathrm{g}} + k_{\mathrm{s}} + 2k^{s}_{\mathrm{g}} & -k_{\mathrm{s}} & 0 \\ -k_{\mathrm{s}} & k_{\mathrm{s}} + k_{\mathrm{b}} + 2k^{s}_{\mathrm{s}} & -k_{\mathrm{b}} \\ 0 & -k_{\mathrm{b}} & k_{\mathrm{b}} + 2k^{s}_{\mathrm{b}} \end{bmatrix}$$

$$\boldsymbol{C^p}=\begin{bmatrix} c_{\rm g}+2c_{\rm g}^s & -c_{\rm s} & 0 \\ 2c_{\rm s}^s & c_{\rm s}+2c_{\rm s}^s & -c_{\rm b} \\ 2c_{\rm b}^s & 2c_{\rm b}^s & c_{\rm b}+2c_{\rm b}^s \end{bmatrix};\boldsymbol{K^p}=\begin{bmatrix} k_{\rm g}+2k_{\rm g}^s & -k_{\rm s} & 0 \\ 2k_{\rm s}^s & k_{\rm s}+2k_{\rm s}^s & -k_{\rm b} \\ 2k_{\rm b}^s & 2k_{\rm b}^s & k_{\rm b}+2k_{\rm b}^s \end{bmatrix};\boldsymbol{C'}=\begin{bmatrix} c_{\rm g}^s & 0 & 0 \\ 0 & c_{\rm s}^s & 0 \\ 0 & 0 & c_{\rm b}^s \end{bmatrix};\boldsymbol{K'}=\begin{bmatrix} k_{\rm g}^s & 0 & 0 \\ 0 & k_{\rm s}^s & 0 \\ 0 & 0 & k_{\rm b}^s \end{bmatrix}$$

$$\boldsymbol{C^{p}}'=\begin{bmatrix} c_{\rm g}^s & 0 & 0 \\ c_{\rm s}^s & c_{\rm s}^s & 0 \\ c_{\rm b}^s & c_{\rm b}^s & c_{\rm b}^s \end{bmatrix};\boldsymbol{K^{p}}'=\begin{bmatrix} k_{\rm g}^s & 0 & 0 \\ k_{\rm s}^s & k_{\rm s}^s & 0 \\ k_{\rm b}^s & k_{\rm b}^s & k_{\rm b}^s \end{bmatrix};d\boldsymbol{F}=\begin{Bmatrix} 0 \\ 0 \\ dQ_{\rm r,m} \end{Bmatrix};d\boldsymbol{\ddot{w}_{\rm m}}=\begin{Bmatrix} d\ddot{w}_{\rm g,m} \\ d\ddot{w}_{\rm s,m} \\ d\ddot{w}_{\rm b,m} \end{Bmatrix};d\boldsymbol{\dot{w}_{\rm m}}=\begin{Bmatrix} d\dot{w}_{\rm g,m} \\ d\dot{w}_{\rm s,m} \\ d\dot{w}_{\rm b,m} \end{Bmatrix};d\boldsymbol{w_{\rm m}}=\begin{Bmatrix} dw_{\rm g,m} \\ dw_{\rm s,m} \\ dw_{\rm b,m} \end{Bmatrix}$$

$$d\boldsymbol{\dot{w}_{\rm m}^p}=\begin{Bmatrix} d\dot{w}_{\rm g,m}^p \\ d\dot{w}_{\rm s,m}^p \\ d\dot{w}_{\rm b,m}^p \end{Bmatrix};d\boldsymbol{w_{\rm m}^p}=\begin{Bmatrix} dw_{\rm g,m}^p \\ dw_{\rm s,m}^p \\ dw_{\rm b,m}^p \end{Bmatrix};d\boldsymbol{\dot{w}_{\rm m-1}}=\begin{Bmatrix} d\dot{w}_{\rm g,m-1} \\ d\dot{w}_{\rm s,m-1} \\ d\dot{w}_{\rm b,m-1} \end{Bmatrix};d\boldsymbol{\dot{w}_{\rm m+1}}=\begin{Bmatrix} d\dot{w}_{\rm g,m+1} \\ d\dot{w}_{\rm s,m+1} \\ d\dot{w}_{\rm b,m+1} \end{Bmatrix};d\boldsymbol{w_{\rm m-1}}=\begin{Bmatrix} dw_{\rm g,m-1} \\ dw_{\rm s,m-1} \\ dw_{\rm b,m-1} \end{Bmatrix}$$

$$d\boldsymbol{w_{\rm m+1}}=\begin{Bmatrix} dw_{\rm g,m+1} \\ dw_{\rm s,m+1} \\ dw_{\rm b,m+1} \end{Bmatrix};d\boldsymbol{\dot{w}_{\rm m-1}^p}=\begin{Bmatrix} d\dot{w}_{\rm g,m-1}^p \\ d\dot{w}_{\rm s,m-1}^p \\ d\dot{w}_{\rm b,m-1}^p \end{Bmatrix};d\boldsymbol{\dot{w}_{\rm m+1}^p}=\begin{Bmatrix} d\dot{w}_{\rm g,m+1}^p \\ d\dot{w}_{\rm s,m+1}^p \\ d\dot{w}_{\rm b,m+1}^p \end{Bmatrix};d\boldsymbol{w_{\rm m-1}^p}=\begin{Bmatrix} dw_{\rm g,m-1}^p \\ dw_{\rm s,m-1}^p \\ dw_{\rm b,m-1}^p \end{Bmatrix};d\boldsymbol{w_{\rm m+1}^p}=\begin{Bmatrix} dw_{\rm g,m+1}^p \\ dw_{\rm s,m+1}^p \\ dw_{\rm b,m+1}^p \end{Bmatrix} \quad (3)$$

where the subscripts b, g and s denote the ballast, subgrade and subballast layers, respectively; subscript m stands for the $m^{\rm th}$ sleeper; superscript p represents the plastic part of the response; $\dot{w}$ and $\ddot{w}$ denote the velocity (m/s) and acceleration (m/s^2) of the substructure layers, respectively; m, c and k represent the vibrating mass (kg), damping coefficient (Ns/m) and normal stiffness (N/m) of the track layers, respectively; k^s and c^s denote the shear stiffness (N/m) and shear damping coefficient (Ns/m), respectively; $dQ_{\rm r,m}$ stands for the rail-seat load increment at $m^{\rm th}$ sleeper (N).

Equation (2) is solved at each time instant, t, for all the sleeper locations considered in the analysis using Newmark's numerical integration method to determine the total response of the track substructure. Note that the geotechnical rheological model used to predict the track response has been previously validated by Punetha et al. (2021).

2.1.2. Vibrating mass, spring, dashpot, and plastic slider element

To solve Equation (2), vibrating mass, spring stiffness, damping coefficient, constitutive relationship for the plastic slider elements of each substructure layer, and the rail-seat load are required. The vibrating mass, spring stiffness, damping coefficient and rail-seat load are calculated using a procedure described by Punetha et al. (2021), which essentially requires the values of parameters such as thickness (h), density (ρ), Young's modulus (E) and Poisson's ratio (v) of the substructure layers. This procedure is also described in Appendix 1.

For the ballast and subballast slider elements, the constitutive relationship is based on an extended version of the Nor-Sand model, which has been derived from the fundamental axioms of the critical state theory (Jefferies, 1993; Jefferies and Shuttle, 2002). It employs an associated flow rule with isotropic hardening plasticity, and the influence of principal stress rotation (PSR) is incorporated by rendering the hardening of the yield surface as a function of PSR angle (which is the angle between major principal stress direction and vertical) (Jefferies et al., 2015; Punetha and Nimbalkar, 2022). The salient features of this relationship are provided in Table 1. This model has been used successfully in the past to reproduce the behaviour of geomaterials such as ballast, subballast, mine tailings and sand (Jefferies and Been, 2015; Punetha et al., 2021).

For subgrade slider elements, the constitutive relationship builds on the elastoplastic model developed by Ma et al. (2017) and Lu et al. (2019). It employs a non-associated flow rule with isotropic hardening plasticity, and the influence of PSR is incorporated by rendering the yield surface, potential surface, and hardening rule as a function of PSR angle (Punetha and Nimbalkar, 2022). Table 2 provides the salient features of this relationship. Note that the constitutive relationships for the slider elements are based on the continuum stress variables (viz., p and q). These stress variables are computed using the modified Boussinesq solutions after converting multiple substructure layers to a single-layered material of equivalent thickness (Hirai, 2008; Odemark, 1949; Poulos and Davis, 1974; Waterways Experiment Station, 1954). This approach of translating the boundary forces to stress variables for the plastic slider elements aligns with the existing techniques (e.g., Di Prisco and Vecchiotti, 2006).

2.2. Additional confinement model

The effect of incorporating 3D cellular geoinclusion in a substructure layer is simulated by modifying the stress state for the reinforced layer. This modification is achieved by adding the extra confinement provided by the geoinclusion to the existing stress state. This section describes a method to evaluate the magnitude of the additional confining pressure provided to the infill material.

As shown in Figure 3(a), the cellular geoinclusion reinforced infill soil tends to deform in the vertical and lateral directions under the application of vertical loads. The inclusion resists the lateral deformation of the infill. Consequently, circumferential stresses are generated along its periphery [see Figure 3(b)], which provide additional confinement to the infill. The magnitude of extra confinement along the lateral orthogonal directions (*x* and *y*) can be determined using the hoop tension theory as:

$$\Delta\sigma_{\mathrm{x}} = \frac{2\sigma_{\mathrm{c,x}} t_{\mathrm{g}}}{D_{\mathrm{g}}} \tag{4}$$

$$\Delta\sigma_{\mathrm{y}} = \frac{2\sigma_{\mathrm{c,y}} t_{\mathrm{g}}}{D_{\mathrm{g}}} \tag{5}$$

where $\Delta\sigma_{\mathrm{x}}$ and $\Delta\sigma_{\mathrm{y}}$ are the additional confining pressures in *x* and *y* directions, respectively; D_{g} and t_{g} are diameter or pocket size and thickness of cellular geoinclusion, respectively; $\sigma_{\mathrm{c,x}}$ and $\sigma_{\mathrm{c,y}}$ are the circumferential stresses in *x* and *y* directions, respectively.

The circumferential stress in the geoinclusion can be evaluated using Hooke's law (Timoshenko and Goodier, 1970):

$$\sigma_\mathrm{c} = \frac{M_\mathrm{m}}{t_\mathrm{g}}\left[\frac{(1-\nu_\mathrm{m})\varepsilon_\mathrm{c} + \nu_\mathrm{m}\varepsilon_\mathrm{r}}{(1+\nu_\mathrm{m})(1-2\nu_\mathrm{m})}\right] \tag{6}$$

where M_m and ν_m are the mobilised modulus and Poisson's ratio of the geoinclusion, respectively; ε_c and ε_r are the circumferential and radial strains in the inclusion, respectively.

On substituting the circumferential stress from Equation (6) into Equations (4) and (5), the magnitude of additional confinement can be computed as (Punetha et al., 2020b):

$$\Delta\sigma_\mathrm{x} = -\frac{2M_\mathrm{m}}{D_\mathrm{g}}\left[\frac{(1-\nu_\mathrm{m})k_\mathrm{c} + \nu_\mathrm{m}}{(1+\nu_\mathrm{m})(1-2\nu_\mathrm{m})}\right]\varepsilon_\mathrm{x} \tag{7}$$

$$\Delta\sigma_\mathrm{y} = -\frac{2M_\mathrm{m}}{D_\mathrm{g}}\left[\frac{(1-\nu_\mathrm{m})k_\mathrm{c} + \nu_\mathrm{m}}{(1+\nu_\mathrm{m})(1-2\nu_\mathrm{m})}\right]\varepsilon_\mathrm{y} \tag{8}$$

where ε_x and ε_y are the strains along *x* and *y* directions in infill (assuming that the infill soil and cellular inclusion deform together); k_c is the ratio of circumferential strain to radial strain. It must be noted that for the sake of simplicity, the shape of the cellular inclusion in this study is assumed to be circular (as opposed to their actual shape, which can be a 3D honeycomb).

2.3. Response prediction for reinforced track

The response of a ballasted railway track reinforced with 3D cellular inclusion is computed by following these steps (see Figure 4):

1. Calculate the vibrating mass (*m*), spring stiffness (*k*) and viscous damping coefficient (*c*) for the three substructure layers and the rail seat load (Q_r) acting at each sleeper location of the track section simulated by the geotechnical rheological model (refer to Appendix 1 and Punetha et al., 2021).

2. Evaluate the stress distribution in the substructure layers at each time instant using the modified Boussinesq approach.
3. For each time instant, check whether the yield criterion of the slider element for any substructure layer is met. If the yield is reached and loading conditions are satisfied, compute the plastic deformations using the constitutive relations for the slider element (see Section 2.1.2). Calculate the additional confinement mobilised by the cellular geoinclusion using the strain accumulated in the lateral and longitudinal directions (see Section 2.2).
4. Solve the dynamic equilibrium equation [Equation (2)] using Newmark's numerical integration scheme to compute the total displacement of the track layers at that time instant.
5. Update the stress state using the magnitude of additional confinement in the lateral orthogonal directions.
6. Repeat steps 3 to 5 till the desired number of wheels or axles have passed the section of a railway line simulated by the geotechnical rheological model.
7. Calculate the total displacement time history.

A MATLAB code is developed to perform all the calculations in the proposed computational method (The MathWorks Inc., 2020).

3. Validation

Limited field data is available on the behaviour of ballasted railway tracks reinforced with cellular geoinclusions under train-induced repetitive loading. Nevertheless, the validity of the proposed computational methodology to accurately simulate the behaviour of reinforced railway tracks is investigated by comparing the predicted results with 3D FE analyses conducted by Satyal et al. (2018). Satyal et al. (2018) developed FE models of ballasted railway tracks with and without geocell reinforcement and studied the effect of factors such as geocell configuration, ballast thickness and subgrade type on the track performance. These FE models were previously validated against the experimental plate loading tests on unreinforced and geocell-reinforced ballast overlying weak subgrade soil (Satyal et al., 2018). The 3D FE model of the ballasted railway track for the unreinforced case is shown in Figure 5. The model consists of a ballast layer overlying a 2 m thick subgrade. The model length along the longitudinal and transverse directions is 1.485 m and 5 m, respectively. The nodes at the bottom boundary of the model were completely fixed, while the nodes along the side boundaries were normally fixed. Only one half of the track was modelled due to symmetry. For the reinforced case, the geocell was modelled as an embedded element inside the ballast layer. Other details of the model can be found in Satyal et al. (2018).

Figure 5 compares the results predicted using the present method and that using FE analyses by Satyal et al. (2018). Table 3 lists the values of the parameters used in the simulation. It can be observed that the results predicted using the proposed approach agree reasonably well with the predictions from the FE analyses. The settlement values evaluated using the present method vary by 1% – 13% from the FE results. The proposed model can accurately predict the reduction in track settlement achieved by reinforcing the bottom of the ballast layer with a geocell. Moreover, the performance of the reinforced track at various subgrade conditions and ballast thicknesses is also predicted satisfactorily.

The validity of the proposed computational methodology is also investigated by comparing the predicted results with the reduced scale model tests conducted by

Banerjee et al. (2020a). The values of the parameters used in the simulation are listed in Table 3. Figure 6 compares the results predicted using the present method with the data reported by Banerjee et al. (2020a). It is apparent that the predicted results are in a reasonable agreement with the model test data. The present method can satisfactorily simulate the settlement reduction caused by reinforcing the subballast layer with geocell at different subballast layer thicknesses. Moreover, it can also capture the improvement in settlement reduction with a decrease in geocell pocket size.

4. Results and discussion

A parametric analysis is carried out to investigate the influence of geoinclusion properties and axle load on the performance of a reinforced ballasted railway track. Subsequently, the effectiveness of 3D cellular and planar [two-dimensional (2D)] geosynthetics in reducing the track settlement is compared. Table 4 summarises the parameters investigated in this study. Table 5 lists the values of input parameters used in the analysis. The nominal values of the variables are provided in the parenthesis. The ballast used in the analysis is crushed basalt (poorly graded gravel), the subballast comprises of well-graded sand with gravel, and the subgrade is fine sand. The properties of the track materials are selected based on published literature (Cai et al., 2015; Li et al., 2016; Li et al., 2018; Punetha et al., 2021; Suiker et al., 2005; Zhai et al., 2004). The thickness of ballast, subballast and subgrade are considered as 0.3 m, 0.15 m, and 6 m, respectively. The results are computed for multiple passages of a train comprising 32 axles with a configuration identical to the Acela express passenger train at a speed of 100 km/h. Only one variable is changed for each analysis, while other parameters are allocated nominal values. The nominal value of axle load is taken as 25 t. The depth of cellular geoinclusion is considered as 150 mm, and it is provided at the bottom of the ballast layer.

4.1. Influence of geoinclusion material

The magnitude of additional confinement provided by a 3D cellular geosynthetic depends on the type of material used for its manufacture. Hence, the material type may influence the inelastic deformation or settlement accumulated in a reinforced track layer. To study its effect, five different types of materials, namely, HDPE, nonwoven polypropylene (PP) geotextile, woven coir geotextile, geocomposite (PP biaxial geogrid with PP fabric) and scrap rubber tyre (with one sidewall removed), are considered in the analysis. Figure 7(a) shows the load-strain curves for the five different materials obtained using tension tests (Biabani, 2015; Gonzalez-Torre et al., 2014; Indraratna et al., 2017; Koerner, 2012; Lal et al., 2017). Figure 7(b) shows the accumulation of track settlement with tonnage when the cellular geoinclusion manufactured using different materials is provided at the bottom of the ballast layer. It can be observed that the track settlement decreases on reinforcing the substructure layer. However, the magnitude of settlement reduction depends on the material used to manufacture the artificial inclusion. The maximum reduction in track settlement is provided by the rubber tyre (32%), followed by geocomposite (30%), HDPE (22%), woven coir geotextile (12.5%) and nonwoven PP geotextile (4%). This observation is reasonable as the rubber tyre provides the maximum confinement among all the materials tested, which is apparent in Figure 8. This figure shows the variation of additional confinement with cumulative tonnage provided by five different materials along the longitudinal, $\Delta\sigma_x$, and transverse directions, $\Delta\sigma_y$. The rubber tyre provides the maximum confinement because the modulus of the rubber tyre is the highest among the five materials considered [see Figure 7(a)]. It is also apparent that the geocomposite provides more confinement than HDPE, woven coir geotextile and nonwoven PP geotextile. This observation is reasonable as the modulus of geocomposite is higher than HDPE, woven coir, and nonwoven PP geotextiles [see Figure 7(a)]. Moreover, the confinement provided along the transverse direction (represented by solid lines) is much higher than that in the longitudinal direction (represented by dashed lines) for all the materials tested. This trend may be attributed to the fact that the deformation is higher in the transverse direction, and consequently, more confinement is mobilised in this direction compared to the longitudinal direction.

Thus, it is apparent that stiffer materials offer more confinement than softer materials. Consequently, cellular geoinclusions made up of stiffer materials provide more improvement in the track performance than those manufactured using softer materials. Nonetheless, the selection of a particular geosynthetic material must be based on factors such as its intended role, the scope of the project, and the costs associated with the fabrication and installation.

4.2. Influence of pocket size

The cellular geoinclusion diameter or pocket size (D_g) is varied between 0.25 m to 0.4 m to investigate its effect on the settlement reduction. Figure 9(a) shows the variation of settlement with depth when the bottom of the ballast layer is reinforced with cellular HDPE inclusion having different diameter or pocket sizes. It can be observed that the track settlement increases with an increase in D_g. The settlement increases by 6% on increasing D_g from 0.25 m to 0.4 m. This observation is reasonable since more material is available per unit area for providing confinement when D_g is smaller. Nevertheless, the track settlement is 17.4% less than the unreinforced case, even when D_g is 0.4 m. Figures 9(b) and 9(c) show similar trends for geoinclusions manufactured using woven coir and nonwoven PP geotextiles, respectively. Thus, the performance of a reinforced track is somewhat sensitive to the diameter or pocket size. Cellular inclusions with smaller pocket size provide better confinement and more settlement reduction than those with larger pocket size.

4.3. Influence of axle load

The axle load, Q_a, is varied from 20 t – 30 t to investigate its influence on the effectiveness of the reinforcement. Figure 10 shows the effect of axle load on the accumulation of track settlement with tonnage for different geoinclusion materials, viz. HDPE, woven coir geotextile and nonwoven PP geotextile. It can be observed that the settlement increases for all the cases with an increase in Q_a. For the unreinforced case, the cumulative settlement after 20 MGT increases by 41.3% on increasing Q_a from 20 t – 30 t. For HDPE inclusion reinforced track, the settlement increases by 37.9% with an increase in Q_a from 20 t – 30 t. This trend is reasonable because the stress transferred to the substructure layers rises on increasing the axle load, leading to an increment in deformation.

It is interesting to note that the effectiveness of reinforcement in reducing the track settlement is relatively constant at the three axle loads. After a cumulative tonnage of 20 MGT, HDPE geoinclusion reduced the settlement by 21%, 22% and 23% for 20 t, 25 t and 30 t axle loads, respectively. Similar behaviour is observed for cellular inclusions manufactured using coir and PP geotextiles. Thus, the results imply that the geoinclusions would maintain their effectiveness in those railway tracks where heavier axle loads are anticipated in the future.

4.4. Comparison with planar geosynthetic reinforcement

This section compares the effectiveness of a 3D-cellular inclusion with a planar (2D) geosynthetic such as geogrid or geotextile. Figure 11(a) shows the equivalence of stress generated in a planar geosynthetic to the extra confining pressure provided to the surrounding soil. The magnitude of additional confinement provided by the planar inclusion can be determined following a similar approach as proposed by Yang and Han (2013) for axisymmetric loading conditions. Since a planar geosynthetic is subjected to 3D loading conditions in a railway track, the additional confinement provided under a 3D stress state can be computed using the following equations:

$$\Delta\sigma_{\mathrm{x}} = -\frac{M_{\mathrm{m}}\alpha_{\mathrm{m}}}{H_{\mathrm{m}}(1-\nu_{\mathrm{m}}^{2})}(\varepsilon_{\mathrm{x}} + \nu_{\mathrm{m}}\varepsilon_{\mathrm{y}}) \tag{9}$$

$$\Delta\sigma_{\mathrm{y}} = -\frac{M_{\mathrm{m}}\alpha_{\mathrm{m}}}{H_{\mathrm{m}}(1-\nu_{\mathrm{m}}^{2})}(\varepsilon_{\mathrm{y}} + \nu_{\mathrm{m}}\varepsilon_{\mathrm{x}}) \tag{10}$$

where α_{m} and H_{m} are the bonding coefficient and influence height of planar geosynthetic. The derivation of Equations (9) and (10) is provided in Appendix 2. H_{m} is assumed as 150 mm in this study, which is equal to the height of 3D cellular geoinclusion. The value of α_{m} depends on several factors such as stiffness and Poisson's ratio of geosynthetic and soil-geosynthetic interface stiffness (see Yang and Han, 2013). For simplicity, α_{m} is varied from 0.25 to 0.75 in the analysis to show its influence on the benefits provided by planar geosynthetics.

Figure 11(b) shows the effectiveness of planar and 3D cellular geosynthetics in reducing the track settlement. For planar case, PP, coir, and HDPE may represent nonwoven PP geotextile, woven coir geotextile and biaxial HDPE geogrid, respectively. It can be observed that the use of both 3D and planar geosynthetics decrease the track settlement; however, the 3D inclusions are more effective in reducing the settlement as compared to planar geosynthetics. After a cumulative tonnage of 20 MGT, the planar PP, coir and HDPE inclusions reduce the track settlement by 2%, 8.6% and 15.3%, respectively, for α_m = 0.25. Whereas the 3D geoinclusions manufactured using PP, coir, and HDPE reduce the track settlement by 4%, 12.5% and 22%, respectively. This finding is reasonable because a 3D cellular inclusion provides confinement to the infill material by resisting its lateral deformation throughout the inclusion height, whereas the confinement provided by a planar geosynthetic depends on the frictional interaction and interlocking with the soil at the interface. It is also apparent that the effectiveness of planar geosynthetic increases with an increase in α_m. The higher the frictional interaction between soil and planar geosynthetic (large value of α_m), the higher is the mobilised confinement and consequently, more settlement is reduced.

5. Application to transition zones

The previous section demonstrated that a considerable reduction in track settlement could be achieved when the granular track layers are reinforced with 3D cellular inclusions. The adequacy of geoinclusions in reducing the differential settlement at the transition zones is investigated in this section. Figure 12 shows the geotechnical rheological model of a typical open track-bridge transition. The substructure of the softer side of the transition consists of three layers (ballast, subballast and subgrade), while the ballast layer supported by concrete bridge deck forms the substructure on the stiffer side. The track layers are simulated as an array of masses connected using elastic springs, viscous dashpots, and plastic slider elements. The concrete bridge deck and the abutment are simulated as fixed supports due to their negligible deformation compared to the soil layers.

The geosynthetic layer is provided up to a distance of 6 m from the bridge (i.e., in the improved zone). The inclusion is 150 mm in height and is provided at the bottom of the ballast layer (as illustrated in Figure 12).

The governing equations of motion for the transition zone can be derived by applying the dynamic equilibrium condition in Figure 12 as:

$$\begin{aligned}\boldsymbol{M}d\ddot{\boldsymbol{w}}_{\mathrm{i}} + \boldsymbol{C}d\dot{\boldsymbol{w}}_{\mathrm{i}} + \boldsymbol{K}d\boldsymbol{w}_{\mathrm{i}} - \boldsymbol{C}^{\boldsymbol{p}}d\dot{\boldsymbol{w}}_{\mathrm{i}}^{\boldsymbol{p}} - \boldsymbol{K}^{\boldsymbol{p}}d\boldsymbol{w}_{\mathrm{i}}^{\boldsymbol{p}} - \boldsymbol{C}'\{d\dot{\boldsymbol{w}}_{\mathbf{i-1}} + d\dot{\boldsymbol{w}}_{\mathbf{i+1}}\} - \boldsymbol{K}'\{d\boldsymbol{w}_{\mathbf{i-1}} + d\boldsymbol{w}_{\mathbf{i+1}}\} \\ + \boldsymbol{C}^{\boldsymbol{p}'}\left\{d\dot{\boldsymbol{w}}_{\mathbf{i-1}}^{\boldsymbol{p}} + d\dot{\boldsymbol{w}}_{\mathbf{i+1}}^{\boldsymbol{p}}\right\} + \boldsymbol{K}^{\boldsymbol{p}'}\left\{d\boldsymbol{w}_{\mathbf{i-1}}^{\boldsymbol{p}} + d\boldsymbol{w}_{\mathbf{i+1}}^{\boldsymbol{p}}\right\} = d\boldsymbol{F}\end{aligned} \tag{11}$$

$$\begin{aligned}m_{\mathrm{b}}^{r}d\ddot{w}_{\mathrm{b,j}} + k_{\mathrm{b}}^{r}\left[dw_{\mathrm{b,j}} - dw_{\mathrm{b,j}}^{p}\right] + c_{\mathrm{b}}^{r}\left[d\dot{w}_{\mathrm{b,j}} - d\dot{w}_{\mathrm{b,j}}^{p}\right] \\ + k_{\mathrm{b}}^{s,r}\left\langle 2\left[dw_{\mathrm{b,j}} - dw_{\mathrm{b,j}}^{p}\right] - \left[dw_{\mathrm{b,j-1}} - dw_{\mathrm{b,j-1}}^{p}\right] - \left[dw_{\mathrm{b,j+1}} - dw_{\mathrm{b,j+1}}^{p}\right]\right\rangle \\ + c_{\mathrm{b}}^{s,r}\left\langle 2\left[d\dot{w}_{\mathrm{b,j}} - d\dot{w}_{\mathrm{b,j}}^{p}\right] - \left[d\dot{w}_{\mathrm{b,j-1}} - d\dot{w}_{\mathrm{b,j-1}}^{p}\right] - \left[d\dot{w}_{\mathrm{b,j+1}} - d\dot{w}_{\mathrm{b,j+1}}^{p}\right]\right\rangle = dQ_{\mathrm{r,j}}^{r}\end{aligned} \tag{12}$$

where superscript r denotes the stiffer side of the transition; subscripts i and j represent the i^{th} and j^{th} sleepers in the softer and stiffer side of the transition, respectively. Equations (11) and (12) are solved using Newmark's integration scheme at each time instant to compute the total response of the transition zone. The effect of reinforcement is simulated using a similar procedure as described in Section 2.3.

The subsequent sections investigate the efficacy of 3D geoinclusions in improving the performance of transition zones through parametric analyses. Table 4 summarises the parameters investigated in this study. Table 5 lists the values of the parameters used in the analyses. The thickness of ballast (in both softer and stiffer sides), subballast and subgrade in the analyses are considered as 0.3 m, 0.15 m, and 6 m, respectively.

5.1. Effect of geoinclusion material

Figure 13 shows the variation of settlement along the track length when 3D geoinclusions manufactured using different materials are provided in the bottom portion of the ballast layer near the bridge approach (improved zone). The results of the unreinforced track are also provided for comparison. Note that the origin of the *x*-coordinate is at the onset of the stiffer side. It can be observed that the differential settlement accumulated after a cumulative tonnage of 20 MGT is the maximum for the unreinforced case. On reinforcing the track, the differential settlement between the stiffer and softer side decreases. The rubber tyre provides the maximum benefit among all the materials tested, followed by geocomposite, HDPE, woven coir geotextile and nonwoven PP geotextile. As discussed in section 4.1, the modulus of rubber tyre at a particular strain value is the highest among all the materials considered; consequently, it provides maximum confinement and improvement in track performance. The reduction in the differential settlement is 5.4%, 16.7%, 29.8%, 40.3% and 43.4% for nonwoven PP geotextile, woven coir geotextile, HDPE, geocomposite and rubber tyre, respectively. Thus, the material used to manufacture the artificial inclusion significantly influences the magnitude of differential settlement at the open track-bridge transition. Stiffer materials provide more performance improvement (or differential settlement reduction) than softer materials.

5.2. Effect of subgrade strength

The subgrade strength is varied by changing the friction angle, φ_c, between 36° and 45°. Figure 14(a) shows the settlement accumulated along the length of the track when cellular HDPE inclusion is provided at the bottom of the ballast layer, and φ_c in the improved zone is varied between 36° and 45°. It can be observed that the reinforcement is more effective when the subgrade strength is high. The differential settlement decreases by 45.3% and 55.6% for φ_c = 40° and 45°, respectively. Figures 14(b) and 14(c) show that the 3D geoinclusions manufactured using woven coir and nonwoven PP geotextiles are also more effective when subgrade strength is high. The differential settlement in the transition zone in the case of coir geotextile decreases by 32.3% and 42.6% for φ_c = 40° and 45°, respectively [see Figure 14(b)]. Similarly, the differential settlement in the case of PP geotextile decreases by 19.4% and 31.2% for φ_c = 40° and 45°, respectively. Thus, the effectiveness of reinforcement significantly depends on the subgrade strength. For critical zones with low subgrade strength, the use of cellular geoinclusion in the ballast layer coupled with subgrade strength increment through ground improvement techniques may prove to be very effective. These findings are in consonance with the results of the experimental investigations conducted by Sol-Sánchez et al. (2015, 2016) on different track configurations which revealed that the track settlement decreases with an increase in strength or bearing capacity of the track layers.

5.3. Effect of reinforcement location

The magnitude of settlement reduction provided by the geosynthetic reinforcement also depends on its location within the rail track. To investigate its most effective placement position, the 3D geoinclusion is provided at three locations in the track, viz., ballast bottom, subballast and subgrade top. Figure 15 shows the variation of settlement along the track length accumulated after a cumulative tonnage of 10 MGT when reinforcement is provided at different locations within the track. As expected, the differential settlement decreases on reinforcing the track layers in the improved zone. The maximum reduction is obtained for the case when the bottom of the ballast layer is reinforced. After a cumulative tonnage of 10 MGT, the differential settlement reduces by 31.6%, 7.4% and 9.7% when the HDPE geoinclusion is provided in the ballast bottom, subballast and subgrade top, respectively. This behaviour is ascribed to a smaller confining pressure acting on the ballast layer prior to the reinforcement (Selig and Waters, 1994). The extra confinement provided by the geoinclusion significantly decreases the deformations in the ballast layer, and consequently, the differential settlement is reduced. The improvement is much smaller when the geoinclusion is provided at the top of the subgrade layer than at the ballast bottom because only the top 0.15 m of the 6 m thick subgrade layer is reinforced. The contribution of the remaining 5.85 m to total settlement is still very high.

Nonetheless, a similar trend is observed for inclusions manufactured using coir geotextile (CG). However, as expected, the HDPE geoinclusion provides more improvement in track performance than the inclusion manufactured using coir geotextile. Thus, the results demonstrate that the performance of a transition zone can be improved with the strategic placement of 3D cellular inclusion in the track.

6. Economic and environmental aspects of 3D cellular geoinclusion reinforcement

The results from this study demonstrate that the use of 3D cellular geoinclusions improves the track performance by reducing the settlement and decreasing the track geometry degradation rate. Consequently, the frequency of periodic maintenance operations can be decreased, leading to significant cost savings. By employing 3D cellular geoinclusions into the track, it is feasible to reduce the thickness of granular layers (such as subballast) without compromising track performance, as illustrated in Figure 16. As evident, the reduction in subgrade settlement is identical when the HDPE geoinclusion is provided at the top of the subgrade and when h_s is increased from 0.15 m to 0.2 m. Thus, by reinforcing the top of the subgrade layer with geoinclusion, the subballast thickness could be reduced by 25%, thereby mitigating the environmental impact while lowering overall costs. This is especially true when a sufficient supply of good quality subballast material is unavailable near the construction site, leading to significant economic and environmental consequences (Sol-Sánchez and D'Angelo, 2017).

The results from this study also revealed that rubber tyres could significantly improve the track performance. The use of scrap rubber tyres as cellular reinforcement can be considered an environment friendly alternative for enhancing track performance because these tyres have become a major source of pollution on a global scale. Around 50 million tyre equivalent passenger units are estimated to be discharged annually in Australia (Farooq et al., 2021). Therefore, reusing these tyres in the railway tracks may be an appealing solution.

Recently, the use of geocells below the ballast layer to improve the load-carrying capacity of soft subgrade has also been recommended in the guidelines such as ARTC RTS 3430 (Australian Rail Track Corporation, 2006). This recommendation is a testimony of interest among the railway industries regarding the use of 3D cellular geosynthetic reinforcement technology in real tracks.

Despite these environmental and economic benefits, there are a few issues pertaining to the use of 3D cellular inclusions in railway tracks. One major concern is the initial cost of synthetic inclusions (made up of HDPE). In this regard, the geoinclusions made of coir geotextile can serve as low-cost alternatives to their synthetic counterparts. Nevertheless, the issues such as the long-term performance of geoinclusions, particularly their fatigue life (Sol-Sánchez and D'Angelo, 2017), and their behaviour under train-induced impact loading (Nimbalkar et al., 2012) continue to require comprehensive research, which constitute the future scope of this study.

7. Conclusions

In this study, a novel computational methodology is developed by integrating the additional confinement model with the geotechnical rheological model to investigate the efficacy of 3D cellular inclusions in improving the performance of ballasted railway tracks. The primary features of the method include:

- Use of simplified yet effective geotechnical rheological model which can incorporate inhomogeneous support conditions along the track length, capture the effect of PSR due to moving wheel loads and accurately predict the settlement accumulated in the track after multiple train passages.
- The utilisation of the additional confinement model derived from hoop stress theory and Hooke’s law that can evaluate the magnitude of extra confinement offered by cellular geosynthetics under 3D loading conditions (or general stress state).
- Provides a simple yet elegant analytical framework (which involves solving governing equations in a step-by-step manner) to evaluate the response of ballasted railway tracks at normal and transition zones while incorporating the effect of geosynthetic reinforcement in contrast to previous studies that relied on the use of commercial software packages, which were often computationally intensive.

The methodology is successfully validated against the results of FE analyses and experimental model tests reported in the literature. A parametric study is carried out to investigate the influence of axle load and geosynthetic properties on the performance of reinforced railway tracks. Subsequently, the methodology is applied to a typical open track-bridge transition, and the adequacy of cellular inclusion in mitigating the differential settlement at the transition is investigated. Finally, the effect of placement location, geosynthetic and subgrade properties on the performance of the transition zone is discussed. The following conclusions can be drawn from this study:

- The material used to manufacture the 3D cellular inclusion significantly influences the reduction in the differential settlement at the open track-bridge transition. Stiffer materials such as rubber tyre, geocomposite and HDPE reduced the differential settlement by 43.4%, 40.3% and 29.8%, respectively. In contrast, softer materials such as woven coir and nonwoven PP geotextiles reduced the differential settlement by 16.7% and 5.4%, respectively.
- Geoinclusions with smaller pocket size are more effective than those with large pocket size.
- The effectiveness of artificial inclusions in reducing the differential settlement depends on the subgrade strength. The reinforcement is more effective when the subgrade strength is high compared to the case when subgrade strength is low.
- The improvement in track performance provided by the cellular geoinclusion also depends on its placement location within the track. In this study, the bottom of the ballast layer is found to be the most effective location for reinforcement.

Thus, the present study demonstrates that 3D cellular geoinclusions effectively reduce the settlement in ballasted railway tracks and possess enormous potential for future use. The essential contribution of this study is the development of a technique that can assist railway engineers in assessing the efficacy of artificial inclusions in enhancing the performance of railway tracks, especially in transition zones. This method may help select the most appropriate placement location, size, and type of geoinclusion for deriving maximum potential benefits and optimising the track performance. The main contribution of this article is the development of an analytical approach to assess the influence of 3D cellular inclusions on the behaviour of ballasted railway tracks. To the authors' knowledge, it is for the first time that a geotechnical rheological model with an enhanced capability to simulate the improvement provided by 3D geoinclusions is used to predict the ballasted track response. The developed methodology is a mechanistic approach in which plastic slider elements are employed to predict the inelastic deformations in the track layers, and the influence of reinforcement is simulated using hoop stress theory and Hooke's law. This approach is a significant advancement over the existing analytical methods that employ empirical equations to capture the inelastic deformations and reinforcement benefits.

Acknowledgements

This research is a part of the AIC-2020-247 project, which was supported by the Australian Government through the Australia-India Council (AIC) of the Department of Foreign Affairs and Trade. The authors wish to thank the anonymous reviewers for providing valuable comments and suggestions.

Appendix 1.

The vibrating mass and spring stiffness of the three substructure layers are evaluated based on the geometry of their effective region, which coincides with a pyramidal load distribution zone below the sleeper bottom (Ahlbeck et al., 1978). This geometry is identified using the parameters such as the thickness of substructure layers, load distribution angles and sleeper dimensions with due consideration to the overlapping of load distribution pyramids along both longitudinal and transverse directions (Punetha et al., 2020a). The vibrating mass is then calculated by multiplying the volume of effective zone of each layer with density. For non-overlapped case, the vibrating mass of the track layers can be calculated as:

$$m_{\mathrm{b}} = \rho_{\mathrm{b}} h_{\mathrm{b}} \left[b_{\mathrm{s}} l_{\mathrm{e}} + (b_{\mathrm{s}} + l_{\mathrm{e}}) h_{\mathrm{b}} \tan \alpha_{\mathrm{b}} + \frac{4}{3} h_{\mathrm{b}}^2 \tan^2 \alpha_{\mathrm{b}} \right] \tag{A1}$$

$$\begin{aligned} m_{\mathrm{s}} = \rho_{\mathrm{s}} h_{\mathrm{s}} \Big[& b_{\mathrm{s}} l_{\mathrm{e}} + (b_{\mathrm{s}} + l_{\mathrm{e}})(2h_{\mathrm{b}} \tan \alpha_{\mathrm{b}} + h_{\mathrm{s}} \tan \alpha_{\mathrm{s}}) + 4h_{\mathrm{b}} \tan \alpha_{\mathrm{b}} \, (h_{\mathrm{b}} \tan \alpha_{\mathrm{b}} \\ & + h_{\mathrm{s}} \tan \alpha_{\mathrm{s}}) + \frac{4}{3} h_{\mathrm{s}}^2 \tan^2 \alpha_{\mathrm{s}} \Big] \end{aligned} \tag{A2}$$

$$\begin{aligned} m_{\mathrm{g}} = \rho_{\mathrm{g}} h_{\mathrm{g}} \Big[& b_{\mathrm{s}} l_{\mathrm{e}} + (b_{\mathrm{s}} + l_{\mathrm{e}})\big(2h_{\mathrm{b}} \tan \alpha_{\mathrm{b}} + 2h_{\mathrm{s}} \tan \alpha_{\mathrm{s}} + h_{\mathrm{g}} \tan \alpha_{\mathrm{g}}\big) + 4(h_{\mathrm{b}} \tan \alpha_{\mathrm{b}} \\ & + h_{\mathrm{s}} \tan \alpha_{\mathrm{s}})(h_{\mathrm{b}} \tan \alpha_{\mathrm{b}} + h_{\mathrm{s}} \tan \alpha_{\mathrm{s}} + h_{\mathrm{g}} \tan \alpha_{\mathrm{g}}) + \frac{4}{3} h_{\mathrm{g}}^2 \tan^2 \alpha_{\mathrm{g}} \Big] \end{aligned} \tag{A3}$$

where subscripts *b*, *s* and *g* denote ballast, subballast and subgrade layers, respectively; *h*, *ρ* and *α* represent the thickness (m), density (kg/m^3) and load distribution angle (°) of the track layers, respectively; l_{e} and b_{s} are the effective length (m) and width (m) of sleeper, respectively. The load distribution angles for the substructure layers are calculated using the following equations:

$$\alpha_{\mathrm{b}} = \tan^{-1} \left\{ \frac{a}{h_{\mathrm{b}}} \left[\sqrt{\frac{\sigma_{\mathrm{slb}}}{\sigma_{\mathrm{bs}}}} - 1 \right] \right\} \tag{A4}$$

$$\alpha_{\mathrm{s}} = \tan^{-1}\left\{\frac{(a + h_{\mathrm{b}}\tan\alpha_{\mathrm{b}})}{h_{\mathrm{s}}}\left[\sqrt{\frac{\sigma_{\mathrm{bs}}}{\sigma_{\mathrm{sg}}}} - 1\right]\right\} \quad \text{(A5)}$$

$$\alpha_{\mathrm{g}} = \tan^{-1}\left\{\frac{(a + h_{\mathrm{b}}\tan\alpha_{\mathrm{b}} + h_{\mathrm{s}}\tan\alpha_{\mathrm{s}})}{h_{\mathrm{g}}}\left[\sqrt{\frac{\sigma_{\mathrm{sg}}}{\sigma_{\mathrm{gr}}}} - 1\right]\right\} \quad \text{(A6)}$$

where σ_{bs}, σ_{sg}, σ_{gr} and σ_{slb} are the vertical stresses (N/m^2) at the ballast-subballast interface, subballast-subgrade interface, bottom of subgrade and sleeper-ballast interface, respectively; a is the equivalent radius of sleeper-ballast contact area (m). The above equations are an extension of the technique used by Han et al. (2011) to the substructure layers.

The spring stiffness of the track layers can be calculated based on the analogy between their effective zone and an axially loaded bar with a non-uniform cross-section. For the non-overlapped case, the stiffness of the substructure layers is computed as:

$$k_{\mathrm{b}} = \frac{2(l_{\mathrm{e}} - b_{\mathrm{s}})E_{\mathrm{b}}\tan\alpha_{\mathrm{b}}}{\ln\left[\frac{l_{\mathrm{e}}}{b_{\mathrm{s}}}\left(\frac{b_{\mathrm{s}} + 2h_{\mathrm{b}}\tan\alpha_{\mathrm{b}}}{l_{\mathrm{e}} + 2h_{\mathrm{b}}\tan\alpha_{\mathrm{b}}}\right)\right]} \quad \text{(A7)}$$

$$k_{\mathrm{s}} = \frac{2(l_{\mathrm{e}} - b_{\mathrm{s}})E_{\mathrm{s}}\tan\alpha_{\mathrm{s}}}{\ln\left[\left(\frac{l_{\mathrm{e}} + 2h_{\mathrm{b}}\tan\alpha_{\mathrm{b}}}{b_{\mathrm{s}} + 2h_{\mathrm{b}}\tan\alpha_{\mathrm{b}}}\right)\left(\frac{b_{\mathrm{s}} + 2h_{\mathrm{b}}\tan\alpha_{\mathrm{b}} + 2h_{\mathrm{s}}\tan\alpha_{\mathrm{s}}}{l_{\mathrm{e}} + 2h_{\mathrm{b}}\tan\alpha_{\mathrm{b}} + 2h_{\mathrm{s}}\tan\alpha_{\mathrm{s}}}\right)\right]} \quad \text{(A8)}$$

$$k_{\mathrm{g}} = \frac{2(l_{\mathrm{e}} - b_{\mathrm{s}})E_{\mathrm{g}}\tan\alpha_{\mathrm{g}}}{\ln\left[\left(\frac{l_{\mathrm{e}} + 2h_{\mathrm{b}}\tan\alpha_{\mathrm{b}} + 2h_{\mathrm{s}}\tan\alpha_{\mathrm{s}}}{b_{\mathrm{s}} + 2h_{\mathrm{b}}\tan\alpha_{\mathrm{b}} + 2h_{\mathrm{s}}\tan\alpha_{\mathrm{s}}}\right)\left(\frac{b_{\mathrm{s}} + 2h_{\mathrm{b}}\tan\alpha_{\mathrm{b}} + 2h_{\mathrm{s}}\tan\alpha_{\mathrm{s}} + 2h_{\mathrm{g}}\tan\alpha_{\mathrm{g}}}{l_{\mathrm{e}} + 2h_{\mathrm{b}}\tan\alpha_{\mathrm{b}} + 2h_{\mathrm{s}}\tan\alpha_{\mathrm{s}} + 2h_{\mathrm{g}}\tan\alpha_{\mathrm{g}}}\right)\right]} \quad \text{(A9)}$$

The damping coefficient for the track layers per unit area can be determined using the following equation (Nimbalkar et al., 2012):

$$c_{\mathrm{b}} = \sqrt{\frac{E_{\mathrm{b}}\rho_{\mathrm{b}}}{(1 + \nu_{\mathrm{b}})(1 - \nu_{\mathrm{b}})}};\ c_{\mathrm{s}} = \sqrt{\frac{E_{\mathrm{s}}\rho_{\mathrm{s}}}{(1 + \nu_{\mathrm{s}})(1 - \nu_{\mathrm{s}})}};\ c_{\mathrm{g}} = \sqrt{\frac{E_{\mathrm{g}}\rho_{\mathrm{g}}}{(1 + \nu_{\mathrm{g}})(1 - \nu_{\mathrm{g}})}} \quad \text{(A10)}$$

The rail seat load is evaluated based on the method described in Doyle (1980):

$$Q_{\mathrm{r,m}}(t) = kS\sum_{j=1}^{a_{\mathrm{t}}} w(x_{\mathrm{m}}^{j}, t) \quad \text{(A11)}$$

where $Q_{r,m}$ denotes the rail seat load at m^{th} sleeper (N) at time instant t; S is the sleeper spacing (m); w is the vertical track deflection (m) computed by solving the beam on elastic foundation equation (see Esveld, 2001); x_m^j is the distance between m^{th} sleeper and j^{th} wheel; a_t is the total number of axles considered; k is the track modulus.

This rail seat load is applied to the ballast surface over a circular sleeper-ballast contact area and the stress distribution below each sleeper is determined using the modified Boussinesq solutions.

Appendix 2.

In planar geosynthetic-reinforced soil, the lateral deformation of the soil under the application of vertical loads generates tensile stresses in the geosynthetic [see Figure 11(a)]. The magnitude of these tensile stresses (T_x and T_y) along *x* and *y* directions can be computed as:

$$T_x = \frac{M_m}{(1 - \nu_m^2)} (\varepsilon_x^m + \nu_m \varepsilon_y^m) \tag{A12}$$

$$T_y = \frac{M_m}{(1 - \nu_m^2)} (\varepsilon_y^m + \nu_m \varepsilon_x^m) \tag{A13}$$

where ε_x^m and ε_y^m are strains in geosynthetic in *x* and *y* directions, respectively. These tensile stresses can be considered as equivalent compressive stresses applied to the soil at the reinforcement location [see Figure 11(a)]. If the equivalent compressive stress is assumed to be distributed uniformly over a thickness of H_m, the extra confining pressure applied to the soil can be computed as:

$$\Delta\sigma_x = \frac{T_x}{H_m} \tag{A14}$$

$$\Delta\sigma_y = \frac{T_y}{H_m} \tag{A15}$$

Substitution of the values of T_x and T_y from Equations (A12) and (A13) to Equations (A14) and (A15), and considering $\alpha_m = -\varepsilon_x^m/\varepsilon_x = -\varepsilon_y^m/\varepsilon_y$ yields Equations (9) and (10).

References

Ahlbeck, D.R., Meacham, H.C., Prause, R.H., 1978. The development of analytical models for railroad track dynamics, in: Kerr, A.D. (Ed.), Railroad Track Mechanics and Technology. Pergamon, London, pp. 239-263.

Australian Rail Track Corporation, 2006. RTS 3430 - Track Reconditioning Guidelines, Engineering Practices Manual - Civil Engineering. Australian Rail Track Corporation, NSW.

Avesani Neto, J.O., 2019. Application of the two-layer system theory to calculate the settlements and vertical stress propagation in soil reinforcement with geocell. Geotextiles and Geomembranes 47, 32-41.

Banerjee, L., Chawla, S., Dash, S.K., 2020a. Application of geocell reinforced coal mine overburden waste as subballast in railway tracks on weak subgrade. Construction and Building Materials 265, 120774.

Banerjee, L., Chawla, S., Dash, S.K., 2020b. Performance Evaluation of Coal Mine Overburden as a Potential Subballast Material in Railways with Additional Improvement Using Geocell. Journal of Materials in Civil Engineering 32, 04020200.

Biabani, M.M., 2015. Behaviour of geocell-reinforced subballast under cyclic loading in plane strain condition, Faculty of Engineering and Information Sciences. University of Wollongong, Wollongong, Australia.

Cai, Y., Sun, Q., Guo, L., Juang, C.H., Wang, J., 2015. Permanent deformation characteristics of saturated sand under cyclic loading. Canadian Geotechnical Journal 52, 795-807.

Chen, C., McDowell, G.R., Thom, N.H., 2012. Discrete element modelling of cyclic loads of geogrid-reinforced ballast under confined and unconfined conditions. Geotextiles and Geomembranes 35, 76-86.

Chrismer, S., 1997. Test of Geoweb to improve track stability over soft subgrade. Association of American Railroads, Washington DC.

Cowland, J., Wong, S., 1993. Performance of a road embankment on soft clay supported on a geocell mattress foundation. Geotextiles and Geomembranes 12, 687–705.

Di Prisco, C., Vecchiotti, M., 2006. A rheological model for the description of boulder impacts on granular strata. Géotechnique 56, 469-482.

Doyle, N.F., 1980. Railway track design: A review of current practice, in: Economics, B.o.T. (Ed.). Bureau of Transport Economics, Australian government publishing service, Canberra, Australia.

Esveld, C., 2001. Modern railway track. MRT-Productions, Delft, The Netherlands.

Farooq, M.A., Nimbalkar, S., Fatahi, B., 2021. Three-dimensional finite element analyses of tyre derived aggregates in ballasted and ballastless tracks. Computers and Geotechnics 136, 104220.

Garga, V.K., O'Shaughnessy, V., 2000. Tire-reinforced earthfill. Part 1: Construction of a test fill, performance, and retaining wall design. Canadian Geotechnical Journal 37, 75-96.

Giroud, J.P., Han, J., 2004. Design method for geogrid-reinforced unpaved roads. II. Calibration and applications. Journal of Geotechnical and Geoenvironmental Engineering 130, 787-797.

Gonzalez-Torre, I., Calzada-Perez, M.A., Vega-Zamanillo, A., Castro-Fresno, D., 2014. Damage evaluation during installation of geosynthetics used in asphalt pavements. Geosynthetics International 21, 377-386.

Han, J., Pokharel, S.K., Yang, X., Manandhar, C., Leshchinsky, D., Halahmi, I., Parsons, R.L., 2011. Performance of geocell-reinforced RAP bases over weak subgrade under full-scale moving wheel loads. Journal of Materials in Civil Engineering 23, 1525-1534.

Hashiguchi, K., 1989. Subloading surface model in unconventional plasticity. International Journal of Solids and Structures 25, 917-945.

Hirai, H., 2008. Settlements and stresses of multi-layered grounds and improved grounds by equivalent elastic method. International Journal for Numerical and Analytical Methods in Geomechanics 32, 523-557.
Indraratna, B., Sun, Q., Grant, J., 2017. Behaviour of subballast reinforced with used tyre and potential application in rail tracks. Transportation Geotechnics 12, 26-36.
Inti, S., Tandon, V., 2021. Design of geocell reinforced roads through fragility modeling. Geotextiles and Geomembranes 49, 1085-1094.
Jefferies, M., Shuttle, D., Been, K., 2015. Principal stress rotation as cause of cyclic mobility. Geotechnical Research 2, 66-96.
Jefferies, M.G., 1993. Nor-Sand: a simple critical state model for sand. Géotechnique 43, 91-103.
Jefferies, M.G., Been, K., 2015. Soil liquefaction: a critical state approach. CRC press, Boca Raton, FL.
Jefferies, M.G., Shuttle, D.A., 2002. Dilatancy in general Cambridge-type models. Géotechnique 52, 625-638.
Kaewunruen, S., Remennikov, A.M., Nguyen, P., Aikawa, A., 2016. Field performance to mitigate impact vibration at railway bridge ends using soft baseplates, The 11th World Congress on Railway Research, 1 ed. WCRR2016, Milan, Italy, pp. 1-10.
Koerner, R.M., 2012. Designing with geosynthetics. Xlibris Corporation.
Kramer, S.L., 1996. Geotechnical Earthquake Engineering. Prentice Hall, New Jersey.
Lal, D., Sankar, N., Chandrakaran, S., 2017. Effect of reinforcement form on the behaviour of coir geotextile reinforced sand beds. Soils and Foundations 57, 227-236.
Leshchinsky, B., Ling, H., 2013a. Effects of geocell confinement on strength and deformation behavior of gravel. Journal of Geotechnical and Geoenvironmental Engineering 139, 340-352.
Leshchinsky, B., Ling, H.I., 2013b. Numerical modeling of behavior of railway ballasted structure with geocell confinement. Geotextiles and Geomembranes 36, 33-43.
Li, D., Hyslip, J., Sussmann, T., Chrismer, S., 2016. Railway geotechnics. Taylor and Francis, Boca Raton, USA.
Li, L., Nimbalkar, S., Zhong, R., 2018. Finite element model of ballasted railway with infinite boundaries considering effects of moving train loads and Rayleigh waves. Soil Dynamics and Earthquake Engineering 114, 147-153.
Liu, Y., Deng, A., Jaksa, M., 2018. Three-dimensional modeling of geocell-reinforced straight and curved ballast embankments. Computers and Geotechnics 102, 53-65.
Liu, Y., Deng, A., Jaksa, M., 2020. Three-Dimensional Discrete-Element Modeling of Geocell-Reinforced Ballast Considering Breakage. International Journal of Geomechanics 20, 04020032.
Lu, D., Li, X., Du, X., Liang, J., 2019. A simple 3D elastoplastic constitutive model for soils based on the characteristic stress. Computers and Geotechnics 109, 229-247.
Ma, C., Lu, D., Du, X., Zhou, A., 2017. Developing a 3D elastoplastic constitutive model for soils: A new approach based on characteristic stress. Computers and Geotechnics 86, 129-140.
Nimbalkar, S., Indraratna, B., 2016. Improved performance of ballasted rail track using geosynthetics and rubber shockmat. Journal of Geotechnical and Geoenvironmental Engineering 142, 04016031.

Nimbalkar, S., Indraratna, B., Dash, S.K., Christie, D., 2012. Improved performance of railway ballast under impact loads using shock mats. Journal of Geotechnical and Geoenvironmental Engineering 138, 281-294.

Nimbalkar, S., Punetha, P., Kaewunruen, S., 2020. Performance improvement of ballasted railway tracks using geocells: present state of the art, in: Sitharam, T.G., Hegde, A., Kolathayar, S. (Eds.), Geocells. Springer Transactions in Civil and Environmental Engineering. Springer, Singapore.

Odemark, N., 1949. Investigations as to the elastic properties of soils and design of pavements according to the theory of elasticity. Statens Vaginstitut, Meddelande 77.

Pokharel, S.K., Han, J., Leshchinsky, D., Parsons, R.L., Halahmi, I., 2010. Investigation of factors influencing behavior of single geocell-reinforced bases under static loading. Geotextiles and Geomembranes 28, 570-578.

Poulos, H.G., Davis, E.H., 1974. Elastic solutions for soil and rock mechanics. John Wiley & Sons, New York.

Punetha, P., Nimbalkar, S., 2022. Geotechnical rheological modeling of ballasted railway tracks considering the effect of principal stress rotation. Canadian Geotechnical Journal.

Punetha, P., Nimbalkar, S., Khabbaz, H., 2020a. Analytical evaluation of ballasted track substructure response under repeated train loads. International Journal of Geomechanics 20, 04020093.

Punetha, P., Nimbalkar, S., Khabbaz, H., 2020b. Evaluation of additional confinement for three-dimensional geoinclusions under general stress state. Canadian Geotechnical Journal 57, 453–461.

Punetha, P., Nimbalkar, S., Khabbaz, H., 2021. Simplified geotechnical rheological model for simulating viscoelasto-plastic response of ballasted railway substructure. International Journal for Numerical and Analytical Methods in Geomechanics 45, 2019-2047.

Rajagopal, K., Krishnaswamy, N.R., Latha, G.M., 1999. Behaviour of sand confined with single and multiple geocells. Geotextiles and Geomembranes 17, 171-184.

Raymond, G.P., 2001. Failure and reconstruction of a gantry crane ballasted track. Canadian Geotechnical Journal 38, 507-529.

Satyal, S.R., Leshchinsky, B., Han, J., Neupane, M., 2018. Use of cellular confinement for improved railway performance on soft subgrades. Geotextiles and Geomembranes 46, 190-205.

Selig, E.T., Waters, J.M., 1994. Track geotechnology and substructure management. Thomas Telford, London.

Simo, J.C., Hughes, T.J.R., 1998. Computational inelasticity. Springer, New York.

Sol-Sánchez, M., D'Angelo, G., 2017. Review of the design and maintenance technologies used to decelerate the deterioration of ballasted railway tracks. Construction and Building Materials 157, 402-415.

Sol-Sánchez, M., Pirozzolo, L., Moreno-Navarro, F., Rubio-Gámez, M.C., 2015. Advanced characterisation of bituminous sub-ballast for its application in railway tracks: The influence of temperature. Construction and Building Materials 101, 338-346.

Sol-Sánchez, M., Pirozzolo, L., Moreno-Navarro, F., Rubio-Gámez, M.C., 2016. A study into the mechanical performance of different configurations for the railway track section: A laboratory approach. Engineering Structures 119, 13-23.

Song, F., Liu, H., Yang, B., Zhao, J., 2019. Large-scale triaxial compression tests of geocell-reinforced sand. Geosynthetics International 26, 388-395.

Suiker, A.S.J., Selig, E.T., Frenkel, R., 2005. Static and cyclic triaxial testing of ballast and subballast. Journal of Geotechnical and Geoenvironmental Engineering 131, 771-782.

The MathWorks Inc., 2020. MATLAB version 2020b. The MathWorks Inc., Natick, Massachusetts.

Timoshenko, S.P., Goodier, J.N., 1970. Theory of elasticity. McGraw Hill, New York.

Wang, H., Markine, V., Liu, X., 2018. Experimental analysis of railway track settlement in transition zones. Proceedings of the Institution of Mechanical Engineers, Part F: Journal of Rail and Rapid Transit 232, 1774-1789.

Waterways Experiment Station, 1954. Investigations of pressures and deflections for flexible pavements: Report no. 4: Homogeneous sand test section. U.S. Waterways Experiment Station, Vicksburg, Mississippi.

Yang, X., Han, J., 2013. Analytical model for resilient modulus and permanent deformation of geosynthetic-reinforced unbound granular material. Journal of Geotechnical and Geoenvironmental Engineering 139, 1443-1453.

Yang, X., Han, J., Leshchinsky, D., Parsons, R.L., 2013. A three-dimensional mechanistic-empirical model for geocell-reinforced unpaved roads. Acta Geotechnica 8, 201-213.

Zarembski, A.M., Palese, J., Hartsough, C.M., Ling, H.I., Thompson, H., 2017. Application of geocell track substructure support system to correct surface degradation problems under high-speed passenger railroad operations. Transportation Infrastructure Geotechnology 4, 106-125.

Zhai, W.M., Wang, K.Y., Lin, J.H., 2004. Modelling and experiment of railway ballast vibrations. Journal of Sound and Vibration 270, 673-683.

Zhou, H., Wen, X., 2008. Model studies on geogrid-or geocell-reinforced sand cushion on soft soil. Geotextiles and Geomembranes 26, 231-238.

Notation

a_h	Cyclic hardening parameter
a_t	Total number of axles considered
b_s	Sleeper width
c_b, c_g, c_s	Viscous damping coefficients for ballast, subgrade and subballast
c_b^{r}	Viscous damping coefficient for ballast in the stiffer side
c_b^{s}, c_g^{s}, c_s^{s}	Shear damping coefficients for ballast, subgrade and subballast
$c_\mathrm{b}^{s,r}$	Shear damping coefficient for ballast in the stiffer side
D_g	Diameter of 3D geoinclusion opening
D^p	Plastic dilatancy
E_b, E_g, E_s	Young’s modulus of ballast, subgrade and subballast

E_b^r	Young's modulus of ballast in the stiffer side
e, e_0	Current and initial void ratio
f_b, f_g, f_s	Yield surface for ballast, subgrade and subballast
f_c, f_r, f_t	Current, reference and transitional subloading surfaces
g	Potential function
H	Hardening parameter in Nor-sand model
H_m	Influence height of planar geosynthetic
h_b, h_g, h_s	Ballast, subgrade and subballast thickness
h_b^r	Ballast thickness in the stiffer side
k	Track modulus
k_b, k_g, k_s	Normal stiffness of ballast, subgrade and subballast
k_b^r	Normal stiffness of ballast in the stiffer side
k_b^s, k_g^s, k_s^s	Shear stiffness of ballast, subgrade and subballast
$k_b^{s,r}$	Shear stiffness of ballast in the stiffer side
k_c	Ratio of circumferential strain to radial strain in geoinclusion
l_e	Effective length of sleeper
M_i	Critical stress ratio corresponding to image state
M_{itc}	Critical stress ratio corresponding to image state for triaxial compression
M_m	Mobilised modulus of geoinclusion
M_{tc}	Critical stress ratio under triaxial compression
$\widehat{M}$	Critical stress ratio in characteristic stress space
m_b, m_g, m_s	Vibrating mass of ballast, subgrade and subballast
m_b^r	Vibrating mass of ballast in the stiffer side
N_v	Volumetric coupling parameter
p	Mean effective stress
p_i	Image mean effective stress
p_{ic}, p_{im}	Hardening parameters
$\hat{p}_{xg}$	Intersection of potential surface with $\hat{p}$ axis
$\hat{p}_{xc}, \hat{p}_{xr}, \hat{p}_{xt}$	Intersection of current, reference and transitional surfaces with $\hat{p}$ axis
Q_w, Q_r	Wheel load and rail-seat load
q	Deviatoric stress

$\hat{q}$ and $\hat{p}$	Deviatoric and hydrostatic stress in characteristic stress space
R, R_{gl}	Parameters that control plastic strain increment under repeated loading
r	Spacing ratio
S	Sleeper spacing
s_t	Settlement of track substructure
$s_{1\alpha}$, $s_{2\alpha}$	Constitutive parameters to account for principal stress rotation effects
T	Cumulative tonnage
T_x, T_y	Tensile stresses in planar geosynthetic along x and y directions
t	Time instant
t_g	Thickness of geoinclusion
$w_{b,m}$, $\dot{w}_{b,m}$, $\ddot{w}_{b,m}$	Displacement, velocity and acceleration of ballast below m^{th} sleeper
$w^{p}_{b,m}$, $\dot{w}^{p}_{b,m}$	Plastic displacement and velocity of ballast below m^{th} sleeper
$w_{s,m}$, $\dot{w}_{s,m}$, $\ddot{w}_{s,m}$	Displacement, velocity and acceleration of subballast below m^{th} sleeper
$w^{p}_{s,m}$, $\dot{w}^{p}_{s,m}$	Plastic displacement and velocity of subballast below m^{th} sleeper
$w_{g,m}$, $\dot{w}_{g,m}$, $\ddot{w}_{g,m}$	Displacement, velocity and acceleration of subgrade below m^{th} sleeper
$w^{p}_{g,m}$, $\dot{w}^{p}_{g,m}$	Plastic displacement and velocity of subgrade below m^{th} sleeper
w^{ve}, w^{p}	Viscoelastic and plastic component of total displacement
x	Distance along longitudinal direction
Z	Plastic softening parameter
z	Depth
α	Angle between major principal stress direction and vertical
α_b, α_s, α_g	Load distribution angles of ballast, subballast and subgrade
α_m	Bonding coefficient
Γ	Critical void ratio at p = 1 kPa
$\Delta\sigma_x$, $\Delta\sigma_y$	Additional confining stress in x and y directions
$d\varepsilon_v^p$, $d\varepsilon_q^p$	Plastic volumetric and deviatoric strain increments
ε_c, ε_r	Circumferential and radial strain
ε_x^m, ε_y^m	Strains in geosynthetic in x and y directions
η, $\hat{\eta}$	Stress ratio in general and characteristic stress space
θ	Lode angle
λ, κ	Slope of critical state and swelling lines in e–ln p space

ν_b, ν_s, ν_g, ν_m	Poisson's ratio of ballast, subballast, subgrade and geoinclusion
ν_b^r	Poisson's ratio of ballast in the stiffer side
ξ, A	Dimensionless material parameters
ρ_b, ρ_g, ρ_s	Density of ballast, subgrade and subballast
ρ_b^r	Density of ballast in the stiffer side
σ_{bs}, σ_{sg}, σ_{slb}	Vertical stresses at the ballast-subballast, subballast-subgrade and sleeper ballast interfaces
$\sigma_{c,x}$, $\sigma_{c,y}$	Circumferential stresses in x and y directions
σ_{gr}	Vertical stress at the bottom of subgrade
σ_j	Principal stress
σ_r	Reference stress
φ_c, φ_e	Critical state friction angles under triaxial compression and extension
χ_i, χ_{tc}	Dilatancy parameters
ψ, ψ_i	State parameters

Tables

Table 1. Salient features of constitutive relationship for ballast and subballast slider elements.

Feature	Mathematical expression	Description
Yield function	$f = \frac{1}{M_\mathrm{i}}\left(\frac{q}{p}\right) + \ln\left(\frac{p}{p_\mathrm{i}}\right) - 1 = g$ where, $M_\mathrm{i} = \left(1 - \frac{N_\mathrm{v}\chi_\mathrm{i}\lvert\psi_\mathrm{i}\rvert}{M_\mathrm{tc}}\right)\left[M_\mathrm{tc} - \frac{M_\mathrm{tc}^2\cos\left(\frac{3\theta}{2}+\frac{\pi}{4}\right)}{3+M_\mathrm{tc}}\right]$ $\chi_\mathrm{i} = \frac{\chi_\mathrm{tc}}{1 - \frac{\lambda\chi_\mathrm{tc}}{M_\mathrm{itc}}}$ $\psi_\mathrm{i} = \psi - \lambda\ln\left(\frac{p}{p_\mathrm{i}}\right)$ $\psi = e - \Gamma + \lambda\ln p$	*f*, *g*: yield and potential functions *q*, *p*: deviatoric and mean effective stresses *i*: image state or at the condition of zero dilatancy N_v: volumetric coupling parameter χ: state-dilatancy parameter ψ: state parameter M_tc: critical stress ratio for triaxial compression θ: Lode angle λ: slope of critical state line (CSL) *e*: void ratio Γ: critical void ratio at p = 1 kPa
Stress-dilatancy	$D^p = \frac{d\varepsilon_\mathrm{v}^p}{d\varepsilon_\mathrm{q}^p} = M_\mathrm{i} - \frac{q}{p}$	$d\varepsilon_\mathrm{v}^p$: plastic volumetric strain increment $d\varepsilon_\mathrm{q}^p$: plastic deviatoric strain increment D^p: plastic dilatancy
Hardening rule	$\frac{dp_\mathrm{i}}{p_\mathrm{i}} = \frac{H}{R_\mathrm{gl}}\frac{M_\mathrm{i}}{M_\mathrm{itc}}\left(\frac{p_\mathrm{i}}{p}\right)_\alpha^{-2}\left[e^{\left(\frac{-\chi_\mathrm{i}\psi_\mathrm{i}}{M_\mathrm{itc}}\right)} - \left(\frac{p_\mathrm{i}}{p}\right)_\alpha\right]d\varepsilon_\mathrm{q}^p$ where, $R_\mathrm{gl} = e^{-\frac{1}{a_\mathrm{h}}\left(1-\frac{p_\mathrm{i}}{p_\mathrm{ic}}\right)}\sqrt{\frac{p_\mathrm{i}-p_\mathrm{im}}{p_\mathrm{ic}-p_\mathrm{im}}}$ $\left(\frac{p_\mathrm{i}}{p}\right)_\alpha = \left(\frac{p_\mathrm{i}}{p} - \frac{1}{r}\right)\left[1 - Z\left(\frac{\lvert d\alpha\rvert}{180}\right)\lvert\psi\rvert\right] + \frac{1}{r}$	dp_i: image mean effective stress increment *H*: plastic hardening parameter p_ic, p_im: internal hardening parameters a_h: cyclic hardening parameter *r*: spacing ratio (assumed as 2.71) *Z*: plastic softening parameter α : angle between major principal stress direction and vertical (°)

Table 2. Salient features of constitutive relationship for subgrade slider elements.

Feature	Mathematical expression	Description
Characteristic stress	$\hat{\sigma}_{\mathrm{j}} = \sigma_{\mathrm{r}} \left(\frac{\sigma_{\mathrm{j}}}{\sigma_{\mathrm{r}}}\right)^{\xi}; j = 1,2,3$ where, $\frac{(1+\sin\varphi_{\mathrm{c}})^{\xi}-(1-\sin\varphi_{\mathrm{c}})^{\xi}}{(1+\sin\varphi_{\mathrm{c}})^{\xi}+2(1-\sin\varphi_{\mathrm{c}})^{\xi}} = \frac{(1+\sin\varphi_{\mathrm{e}})^{\xi}-(1-\sin\varphi_{\mathrm{e}})^{\xi}}{2(1+\sin\varphi_{\mathrm{e}})^{\xi}+(1-\sin\varphi_{\mathrm{e}})^{\xi}}$	'^': parameter in characteristic stress space σ_{j}: principal stress σ_{r}: reference stress (1 kPa) φ_{c}, φ_{e}: critical state friction angles under triaxial compression and extension ξ : dimensionless characteristic stress parameter
Yield function	$f = \frac{(\lambda-\kappa)}{\xi(1+e_0)}\left\{\frac{\bar{A}}{(2-Z_{\alpha})}\ln\left[\frac{(\hat{\eta}^2+\hat{M}_{\alpha}^2)+(1-Z_{\alpha})(\hat{\eta}^2-\hat{M}_{\alpha}^2)}{(\hat{\eta}_0^2+\hat{M}_{\alpha}^2)+(1-Z_{\alpha})(\hat{\eta}_0^2-\hat{M}_{\alpha}^2)}\right] + \ln\left(\frac{\hat{p}}{\hat{p}_0}\right)\right\} - \int \frac{d\varepsilon_{\mathrm{v}}^{p}}{R} = 0$ where, $\hat{M}_{\alpha} = \hat{M}(1-s_{1\alpha}U_{\alpha})$ $Z_{\alpha} = 1 + s_{2\alpha}U_{\alpha}$ $U_{\alpha} = \begin{cases} 1-\cos(2\alpha), & \text{for } 0 \le \alpha \le 45° \\ 1-\cos(2\lvert\alpha\rvert-\pi), & \text{for } 45° \le \lvert\alpha\rvert \le 90° \end{cases}$ $\hat{M} = 3\frac{(1+\sin\varphi_c)^{\xi}-(1-\sin\varphi_c)^{\xi}}{2(1-\sin\varphi_c)^{\xi}+(1+\sin\varphi_c)^{\xi}}$ $\bar{A} = A\frac{(2-Z_{\alpha})\ln 2}{\ln\left(\frac{2}{Z_{\alpha}}\right)}$ $R = e^{-\frac{1}{a_{\mathrm{h}}(1+2U_{\alpha})}\left(1-\frac{\hat{p}_{\mathrm{xc}}}{\hat{p}_{\mathrm{xr}}}\right)}\sqrt{\frac{\hat{p}_{\mathrm{xc}}-\hat{p}_{\mathrm{xt}}}{\hat{p}_{\mathrm{xr}}-\hat{p}_{\mathrm{xt}}}}$	λ: slope of CSL κ: slope of swelling line e: void ratio p: mean effective stress subscript '0': initial value $d\varepsilon_{\mathrm{v}}^{p}$: plastic volumetric strain increment A: dimensionless spacing parameter η: stress ratio $s_{1\alpha}$, $s_{2\alpha}$: constitutive parameters to account for the effects of PSR α : angle between major principal stress direction and vertical (°) a_{h}: cyclic hardening parameter
Potential function	$g = \ln\left[1+\frac{(2\xi-Z_{\alpha})}{Z_{\alpha}}\frac{\hat{\eta}^2}{\hat{M}_{\alpha}^2}\right] + \frac{(2\xi-Z_{\alpha})}{\xi}\ln\left(\frac{\hat{p}}{\hat{p}_{\mathrm{xg}}}\right)$	$\hat{p}_{\mathrm{xg}}$: intersection of potential surface with $\hat{p}$ axis
Hardening[1]	$f_c = \frac{\bar{A}}{(2-Z_{\alpha})}\ln\left[\frac{(\hat{\eta}^2+\hat{M}_{\alpha}^2)+(1-Z_{\alpha})(\hat{\eta}^2-\hat{M}_{\alpha}^2)}{Z_{\alpha}\hat{M}_{\alpha}^2}\right] + \ln\left(\frac{\hat{p}}{\hat{p}_{\mathrm{xc}}}\right)$ $f_{\mathrm{r}} = \frac{\bar{A}}{(2-Z_{\alpha})}\ln\left[\frac{(\hat{\eta}^2+\hat{M}_{\alpha}^2)+(1-Z_{\alpha})(\hat{\eta}^2-\hat{M}_{\alpha}^2)}{Z_{\alpha}\hat{M}_{\alpha}^2}\right] + \ln\left(\frac{\hat{p}}{\hat{p}_{\mathrm{xr}}}\right)$ $f_t = \frac{\bar{A}}{(2-Z_{\alpha})}\ln\left[\frac{(\hat{\eta}^2+\hat{M}_{\alpha}^2)+(1-Z_{\alpha})(\hat{\eta}^2-\hat{M}_{\alpha}^2)}{Z_{\alpha}\hat{M}_{\alpha}^2}\right] + \ln\left(\frac{\hat{p}}{\hat{p}_{\mathrm{xt}}}\right)$	Number of subloading surfaces: 3 $f_{\mathrm{c}}, f_{\mathrm{r}}, f_{\mathrm{t}}$: current, reference and transitional subloading surfaces $\hat{p}_{\mathrm{xc}}, \hat{p}_{\mathrm{xr}}, \hat{p}_{\mathrm{xt}}$: intersection of current, reference and transitional surfaces with $\hat{p}$ axis

[1]based on concept of subloading surfaces (see Hashiguchi, 1989)

Table 3. Input parameters used in the validation.

Layer	Variable	Symbol	Unit	Satyal et al. (2018)	Banerjee et al. (2020a)
Ballast	Young's modulus	E_b	MPa	30	5.99
	Poisson's ratio	ν_b	–	0.4	0.35
	Shear stiffness	k_b^s	MN/m	78.4*	78.4*
	Density	ρ_b	kg/m^3	1500	1621
	Thickness	h_b	m	0.45 – 0.6	0.0875
	Reference void ratio on CSL	Γ	–	1.4*	1.4*
	Slope of CSL	λ	–	0.1*	0.1*
	Critical stress ratio	M_tc	–	1.42†	1.25*
	Volumetric coupling parameter	N_v	–	0.2*	0.2*
	State-dilatancy parameter	χ_tc	–	3*	3*
	Cyclic hardening parameter	a_h	–	0.32†	–
	Plastic hardening parameter	H	–	50-250$\times\psi^*$	50-250$\times\psi^*$
Subballast	Young's modulus	E_s	MPa	–	1.48 – 1.54
	Poisson's ratio	ν_s	–	–	0.32
	Shear stiffness	k_s^s	MN/m	–	476*
	Density	ρ_s	kg/m^3	–	1417
	Thickness	h_s	m	–	0.1125 – 0.15
	Reference void ratio on CSL	Γ	–	–	1.2$^\#$
	Slope of CSL	λ	–	–	0.05$^\#$
	Critical stress ratio	M_tc	–	–	1.65$^\#$
	Volumetric coupling parameter	N_v	–	–	0.5$^\#$
	State-dilatancy parameter	χ_tc	–	–	2.5$^\#$
	Plastic hardening parameter	H	–	–	80-260$\times\psi^\#$
Subgrade	Young's modulus	E_g	MPa	8.5	1.07 – 1.14
	Poisson's ratio	ν_g	–	0.35	0.49
	Shear stiffness	k_g^s	MN/m	1600*	1600*
	Density	ρ_g	kg/m^3	2162	1551
	Thickness	h_g	m	2	0.3625 – 0.4
	Slope of CSL	λ	–	0.0041†	0.06†
	Slope of swelling line	κ	–	0.002†	0.03†
	Critical state friction angle	φ_c	°	37.5 (S1)† 42.5 (S2)†	42.5†
	Characteristic stress parameter	ξ	–	0.1†	0.1†
	Spacing parameter	A	–	0.1†	0.15†
	Cyclic hardening parameter	a_h	–	0.09†	–
Geoinclusion	Material	–	–	PE[1]	Geogrid
	Diameter	D_g	m	0.3	0.1 – 0.165
	Poisson's ratio	ν_m	–	0.35	0.2

[1]Polyethylene, *value taken from Punetha et al. (2021), $^\#$calibrated using triaxial test data reported by Banerjee et al. (2020b), †value selected based on engineering judgement

Table 4. Summary of the parameters studied.

Track section	Parameter	Range or value	Output variable
Regular or standard	Geoinclusion material[1]	HDPE, nonwoven PP geotextile, woven coir geotextile, geocomposite, rubber tyre	Settlement, additional confinement
	Geoinclusion pocket size[2]	0.25 m – 0.4 m	Settlement
	Axle load	20 t – 30 t	Settlement
	Geoinclusion type	Planar (2D), 3D cellular	Settlement
Transition zone	Geoinclusion material[1]	HDPE, nonwoven PP geotextile, woven coir geotextile, geocomposite, rubber tyre	Differential settlement
	Subgrade strength	φ_c = 36° – 45°	Differential settlement
	Reinforcement location	Ballast bottom, subballast, subgrade top	Differential settlement

[1]mobilised modulus of geoinclusion is varied based on the load versus strain curves for different materials, [2]values lie within the range of equivalent pocket size of commercially available geocells

Table 5. Input parameters used in the parametric study.

Layer	Variable	Symbol	Unit	Value
Ballast	Young's modulus[#]	E_b (=E_b^r)	MPa	200
	Poisson's ratio[*]	ν_b (=ν_b^r)	–	0.3
	Shear stiffness[*]	k_b^s (=$k_b^{s,r}$)	MN/m	78.4
	Density[*]	ρ_b (=ρ_b^r)	kg/m^3	1760
	Reference void ratio on CSL[1]	Γ	–	1.4
	Slope of CSL[1]	λ	–	0.1
	Critical stress ratio[1]	M_{tc}	–	1.25
	Volumetric coupling parameter[1]	N_v	–	0.2
	State-dilatancy parameter[1]	χ_{tc}	–	3
	Cyclic hardening parameter	a_h	–	0.3
	Plastic hardening parameter[1]	H	–	50-250$\times\psi$
	Plastic softening parameter[4]	Z	–	10
Subballast	Young's modulus[#]	E_s	MPa	115
	Poisson's ratio[*]	ν_s	–	0.4
	Shear stiffness[*]	k_s^s	MN/m	476
	Density[*]	ρ_s	kg/m^3	1920
	Reference void ratio on CSL[1]	Γ	–	0.9
	Slope of CSL[1]	λ	–	0.05
	Critical stress ratio[1]	M_{tc}	–	1.15
	Volumetric coupling parameter[1]	N_v	–	0.3
	State-dilatancy parameter[1]	χ_{tc}	–	4.2
	Cyclic hardening parameter[1]	a_h	–	0.185
	Plastic hardening parameter[1]	H	–	160-260$\times\psi$
	Plastic softening parameter[4]	Z	–	20
Subgrade	Young's modulus[*†]	E_g	MPa	20
	Poisson's ratio[*]	ν_g	–	0.45
	Shear stiffness[*]	k_g^s	MN/m	1600
	Density[*]	ρ_g	kg/m^3	1920
	Slope of CSL[2]	λ	–	0.0041
	Slope of swelling line[2]	κ	–	0.002
	Critical state friction angle[2]	φ_c	°	36 – 45 (36)
	Characteristic stress parameter[2]	ξ	–	0.1
	Spacing parameter[2]	A	–	0.1
	Cyclic hardening parameter[2]	a_h	–	0.03
	Parameter to account for PSR[2]	$s_{1\alpha}$		0.7
	Parameter to account for PSR[2]	$s_{2\alpha}$		0.05
Geoinclusion	Material	–	–	HDPE, PP geotextile, coir geotextile, geocomposite, rubber tyre
	Diameter[3]	D_g	m	0.25 – 0.4 (0.25)
	Poisson's ratio	ν_m	–	0.3

[1]calibrated using cyclic triaxial test data reported by Suiker et al. (2005), [2]calibrated using hollow cylindrical torsional test data reported by Cai et al. (2015), [3]D_g = 1 m for rubber tyre, [4]value taken from Punetha and Nimbalkar (2022), [#]value adopted from Li et al. (2018), [*]value taken from Punetha et al. (2021), [†]based on range reported by Li et al. (2016)

Figure Captions

Figure 1. Differential settlement in an open track-bridge transition and its potential mitigation using 3D cellular geoinclusion.

Figure 2. Simplified geotechnical rheological model of a ballasted railway track.

Figure 3. (a) Deformation of cellular geoinclusion under the application of vertical load; **(b)** stress profile of the inclusion.

Figure 4. Flowchart to predict the response of ballasted railway track reinforced with 3D cellular inclusion.

Figure 5. Comparison of track settlement computed using present method with results from FE analysis conducted by Satyal et al. (2018).

Figure 6. Comparison of results computed using the present method with experimental data reported by Banerjee et al. (2020a).

Figure 7. (a) Load versus strain curves for five geoinclusion materials obtained from tension tests; **(b)** accumulation of settlement with tonnage for tracks reinforced with cellular inclusions manufactured using different materials.

Figure 8. Variation of additional confinement with tonnage for tracks reinforced with 3D artificial inclusions manufactured using different materials.

Figure 9. Influence of opening or pocket size on track response for 3D cellular geoinclusions manufactured using **(a)** HDPE; **(b)** woven coir geotextile; **(c)** nonwoven PP geotextile.

Figure 10. Influence of axle load on settlement for track reinforced with different cellular inclusion types.

Figure 11. (a) Equivalence of stresses in planar geosynthetic to additional confining pressure in soil; **(b)** comparison of settlement accumulated in the unreinforced track and track reinforced using planar and 3D geosynthetics.

Figure 12. Geotechnical rheological model of a typical open track-bridge transition with 3D cellular geosynthetic reinforcement.

Figure 13. Variation of settlement along the length for unreinforced and reinforced track.

Figure 14. Influence of subgrade strength on effectiveness of artificial inclusions manufactured using: **(a)** HDPE; **(b)** woven coir geotextile; **(c)** nonwoven PP geotextile.

Figure 15. Variation of settlement along the length when 3D cellular inclusion is provided at different positions within the track.

Figure 16. Reduction in subgrade settlement when cellular geoinclusion is provided at the top of the subgrade and when subballast thickness is increased from 0.15 m to 0.3 m.

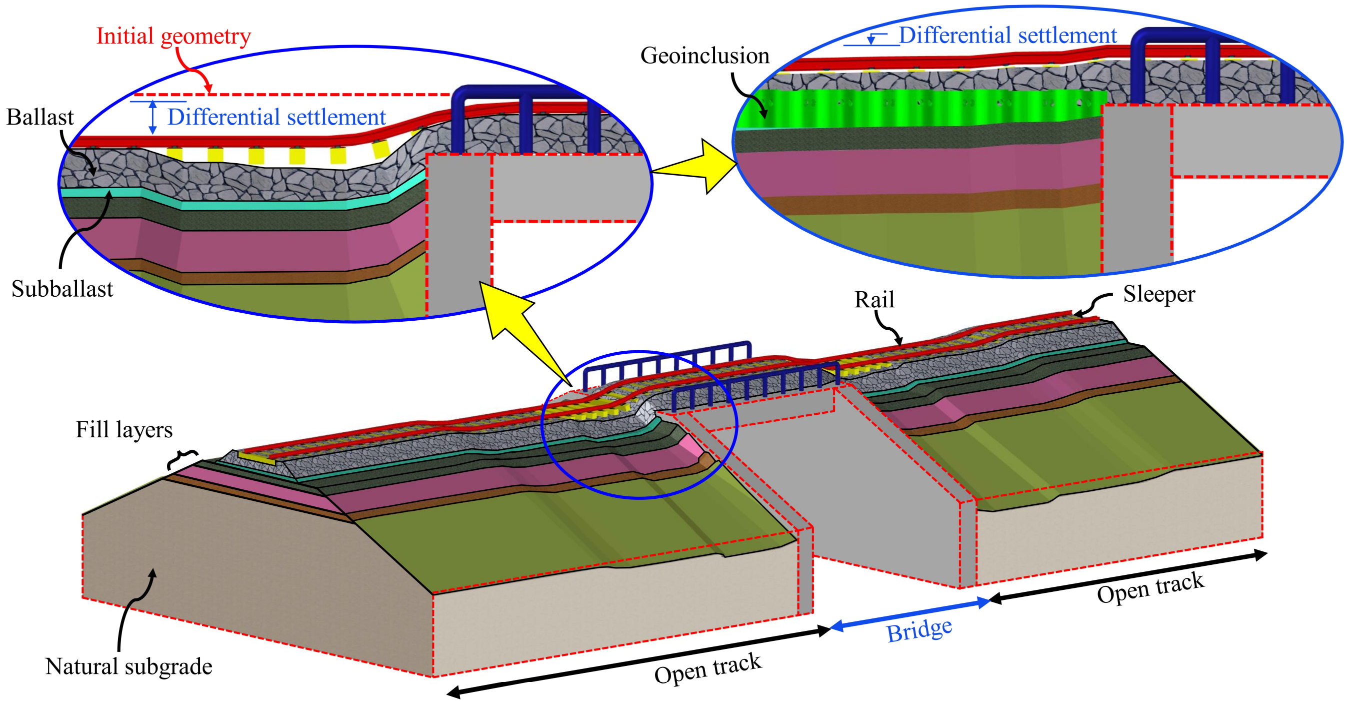

Figure 1. Differential settlement in an open track-bridge transition and its potential mitigation using 3D cellular geoinclusion.

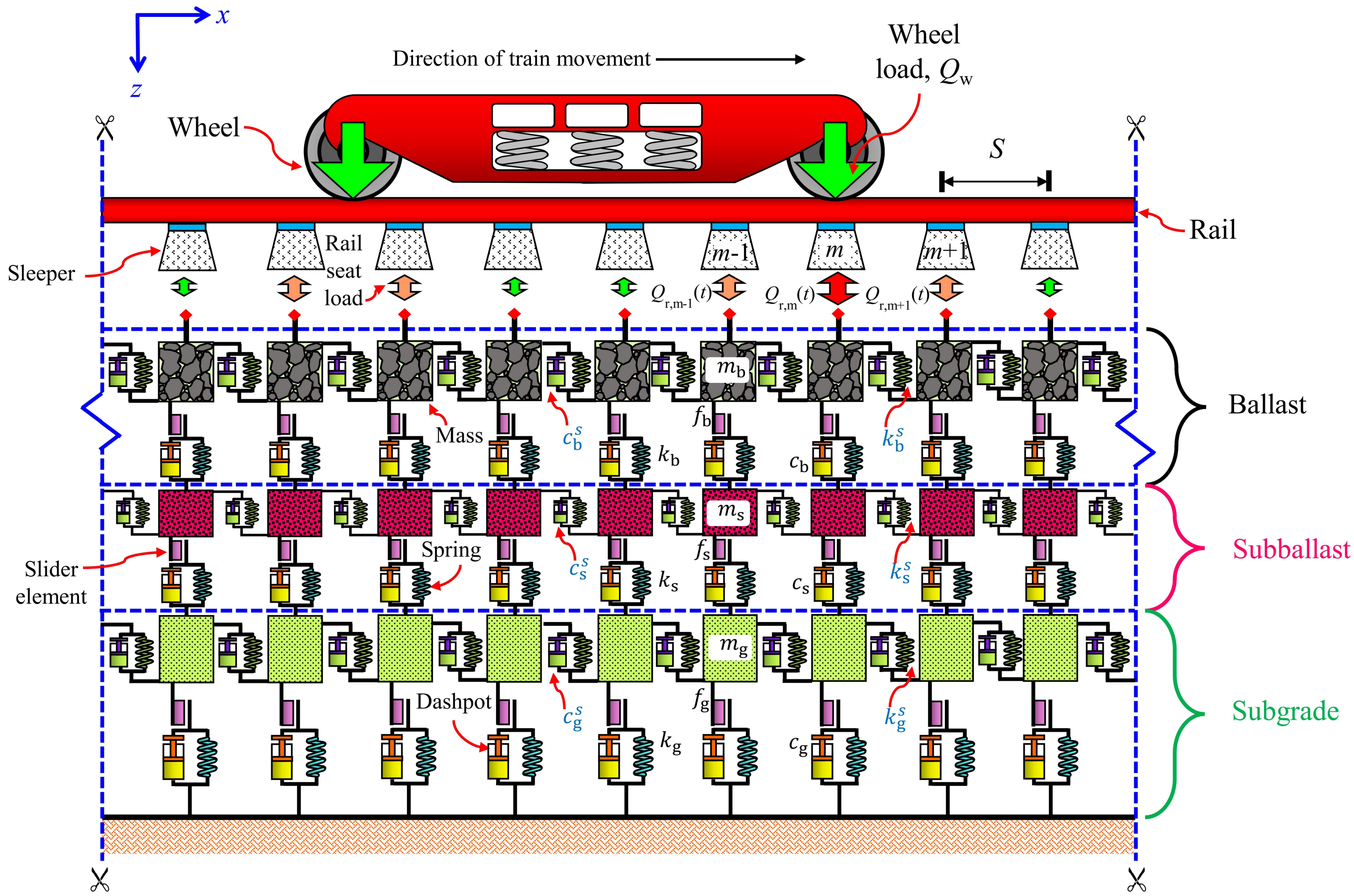

Figure 2. Simplified geotechnical rheological model of a ballasted railway track.

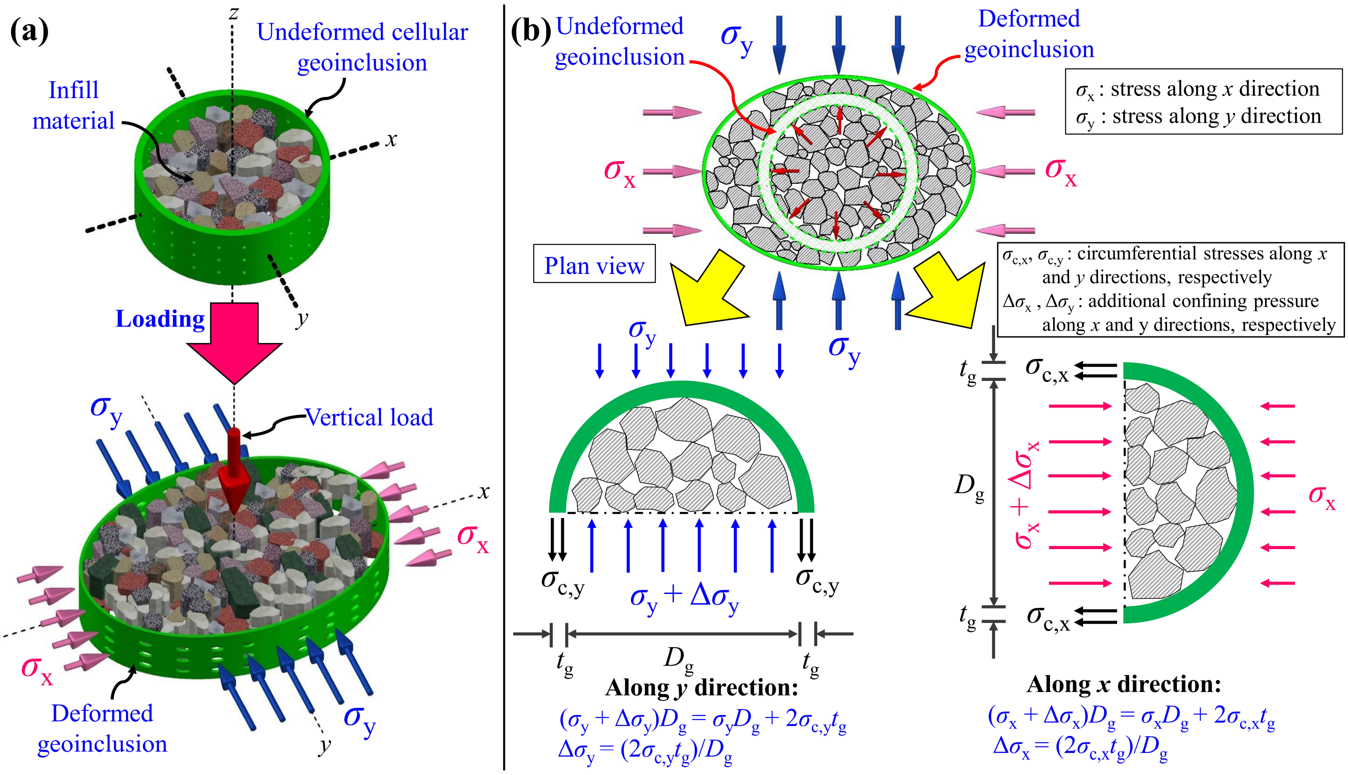

Figure 3. (a) Deformation of cellular geoinclusion under the application of vertical load; **(b)** stress profile of the inclusion.

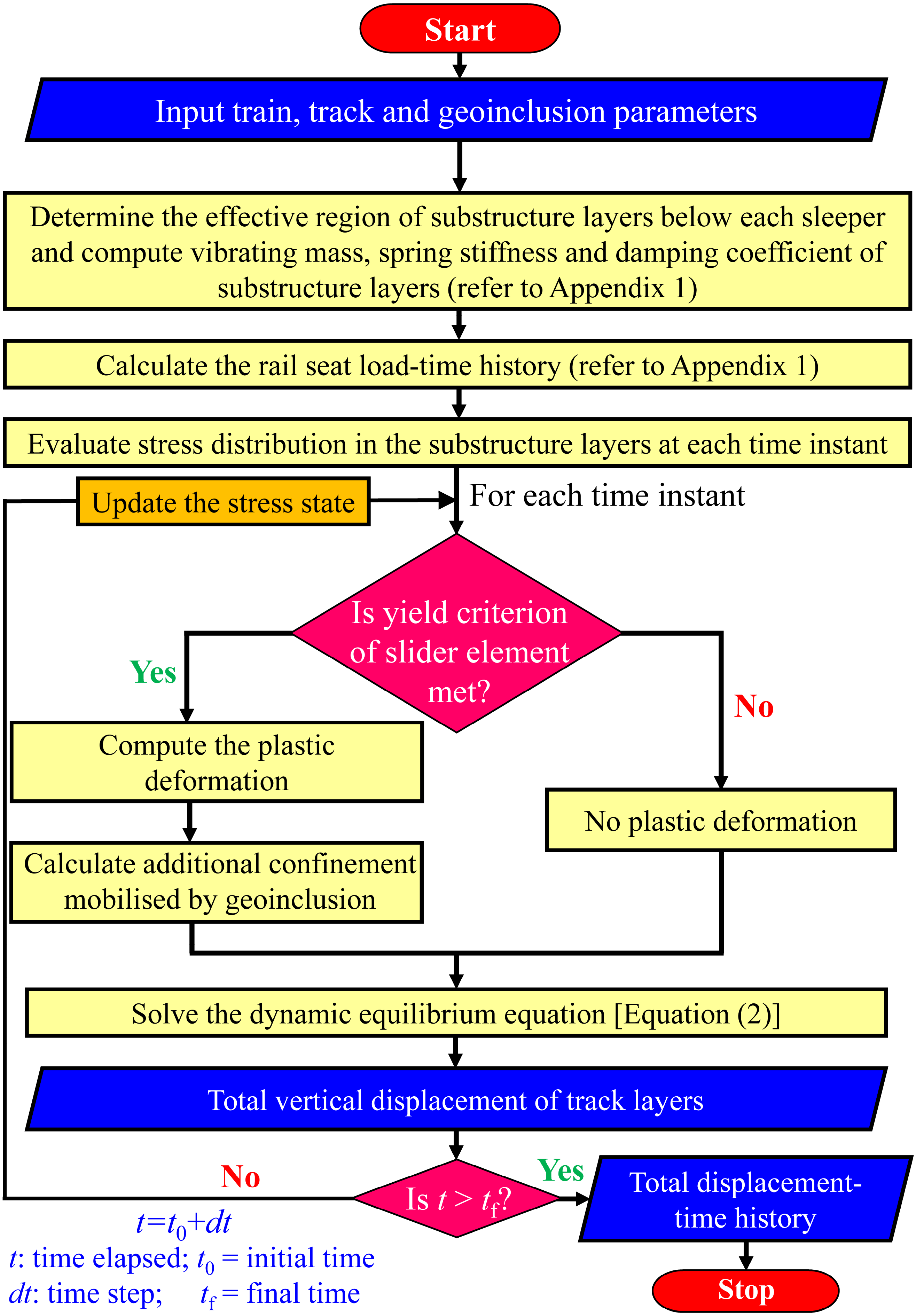

Figure 4. Flowchart to predict the response of ballasted railway track reinforced with 3D cellular inclusion.

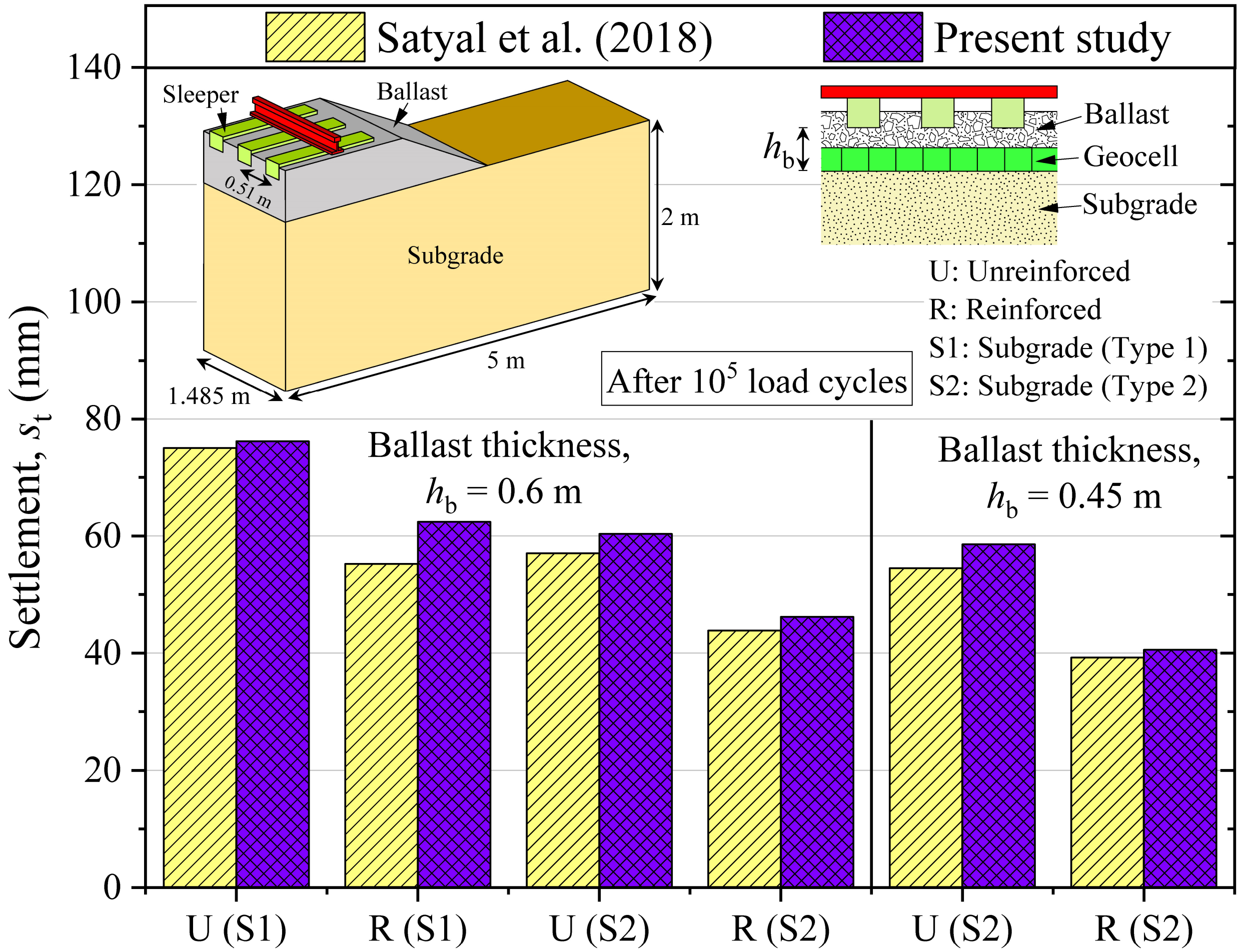

Figure 5. Comparison of track settlement computed using present method with results from FE analysis conducted by Satyal et al. (2018).

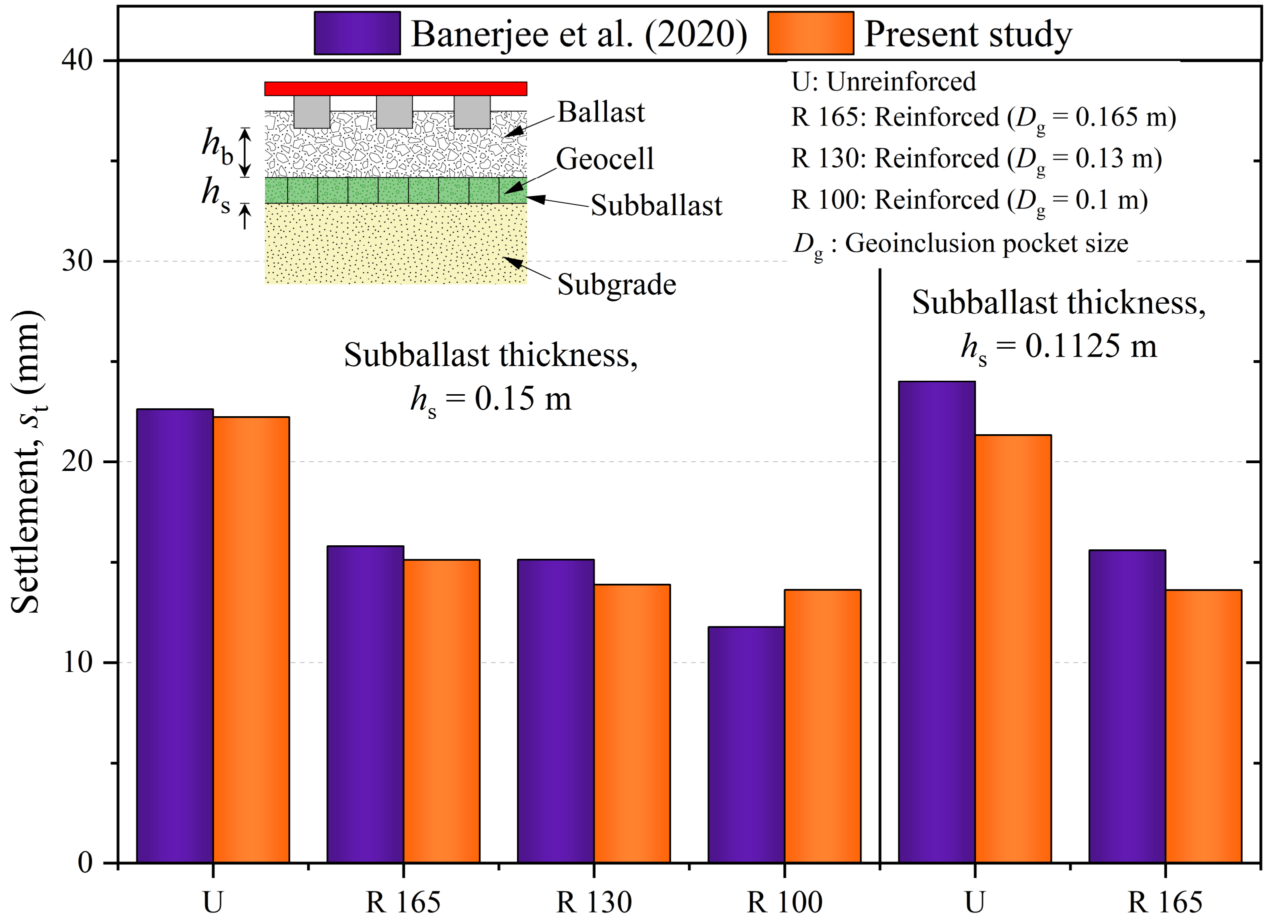

Figure 6. Comparison of results computed using the present method with experimental data reported by Banerjee et al. (2020a).

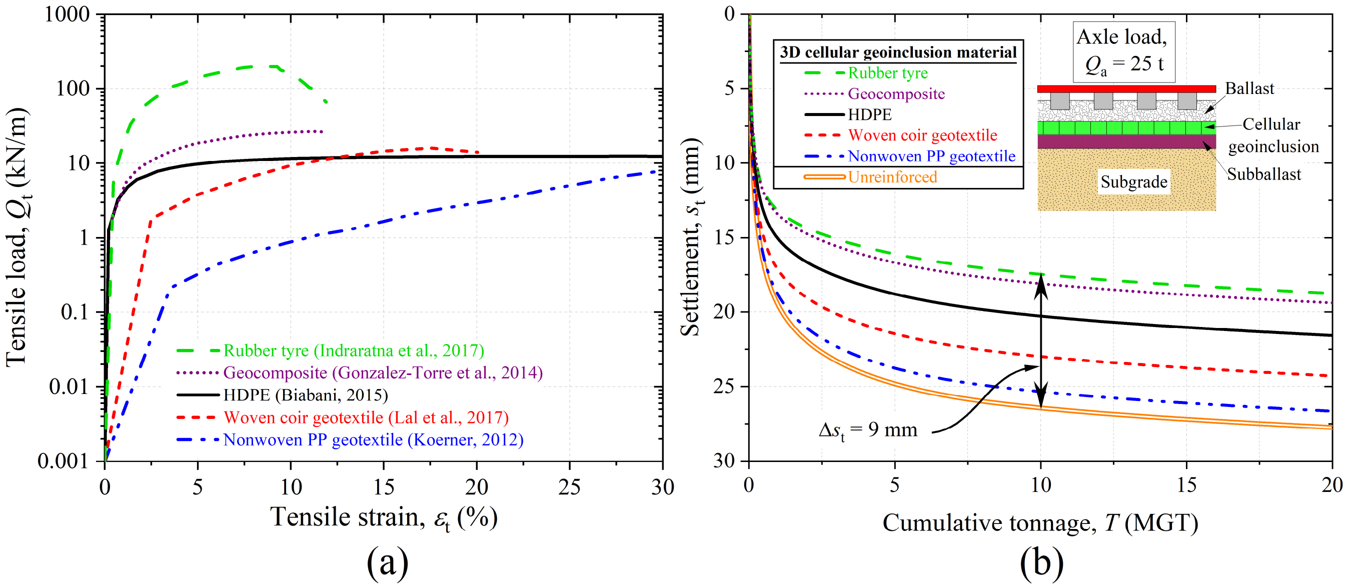

Figure 7. (a) Load versus strain curves for five geoinclusion materials obtained from tension tests; **(b)** accumulation of settlement with tonnage for tracks reinforced with cellular inclusions manufactured using different materials.

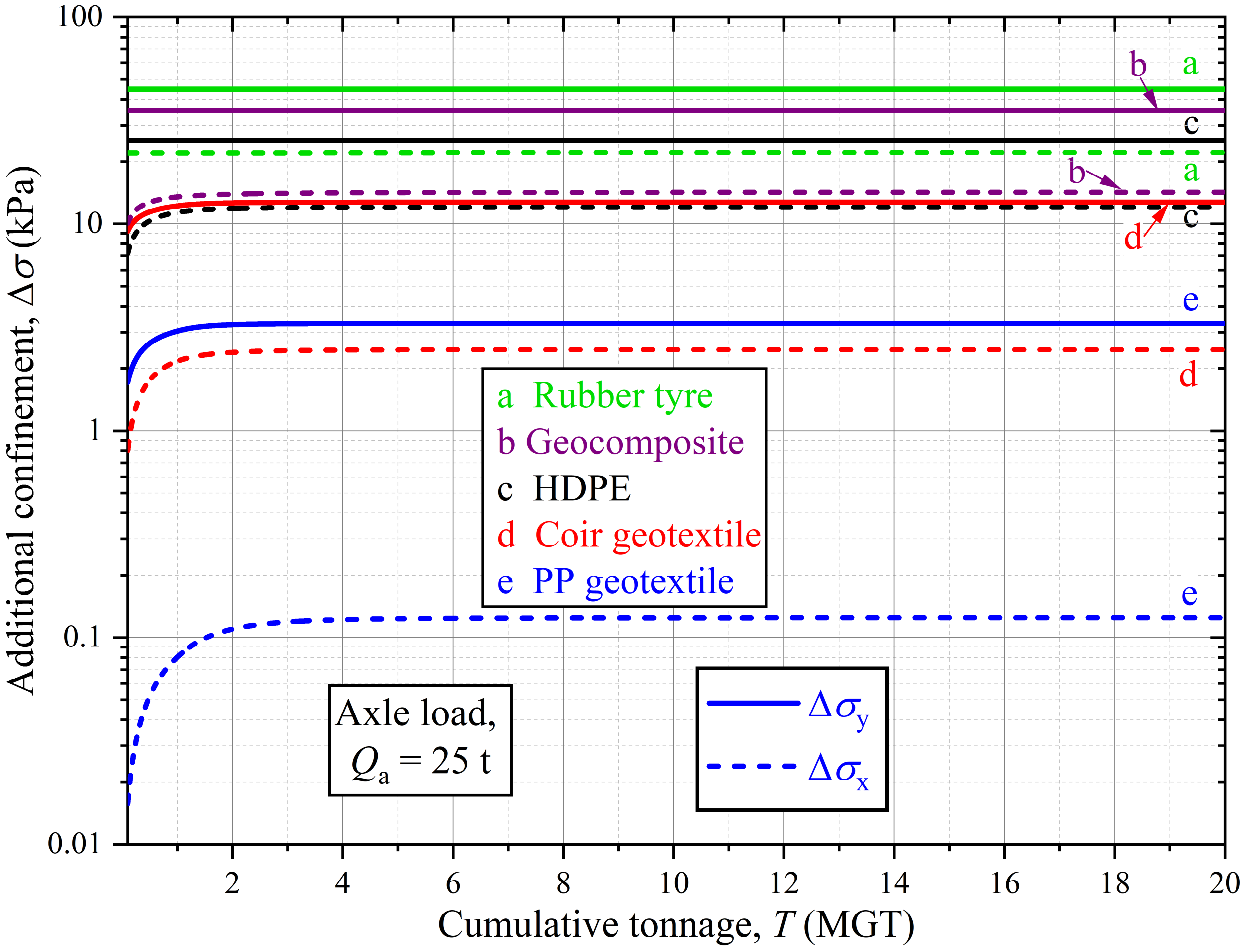

Figure 8. Variation of additional confinement with tonnage for tracks reinforced with 3D artificial inclusions manufactured using different materials.

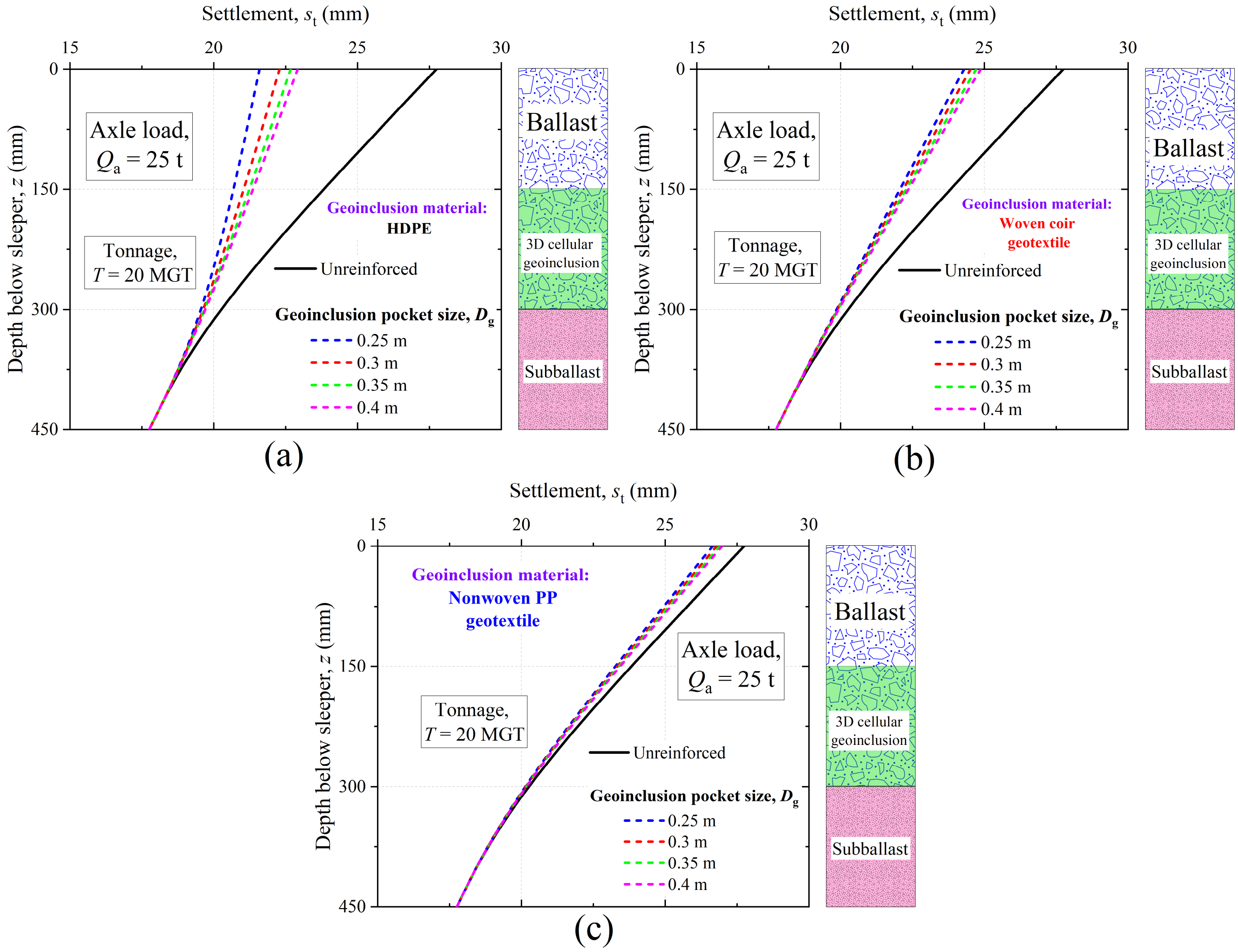

Figure 9. Influence of opening or pocket size on track response for 3D cellular geoinclusions manufactured using **(a)** HDPE; **(b)** woven coir geotextile; **(c)** nonwoven PP geotextile.

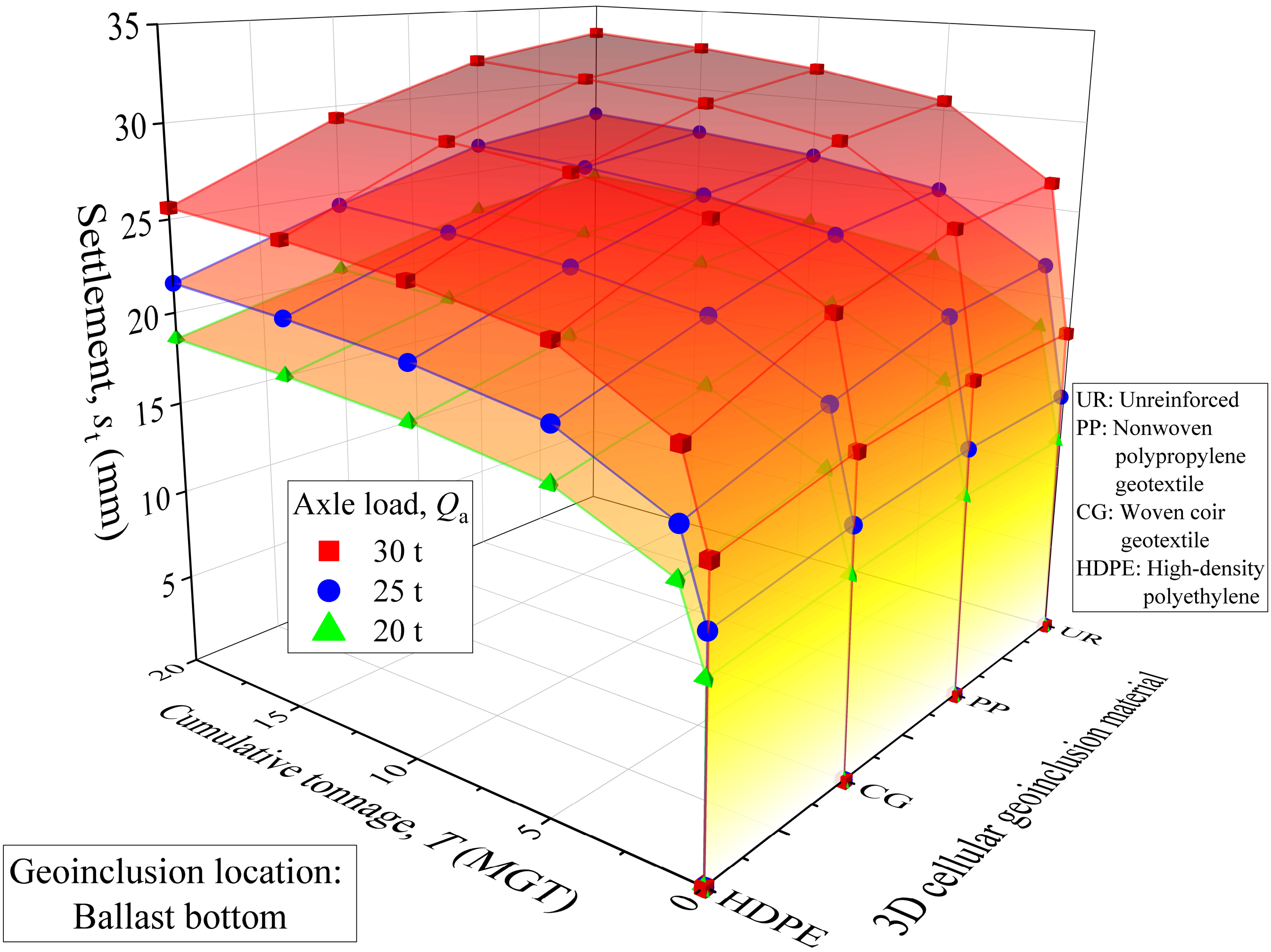

Figure 10. Influence of axle load on settlement for track reinforced with different cellular inclusion types.

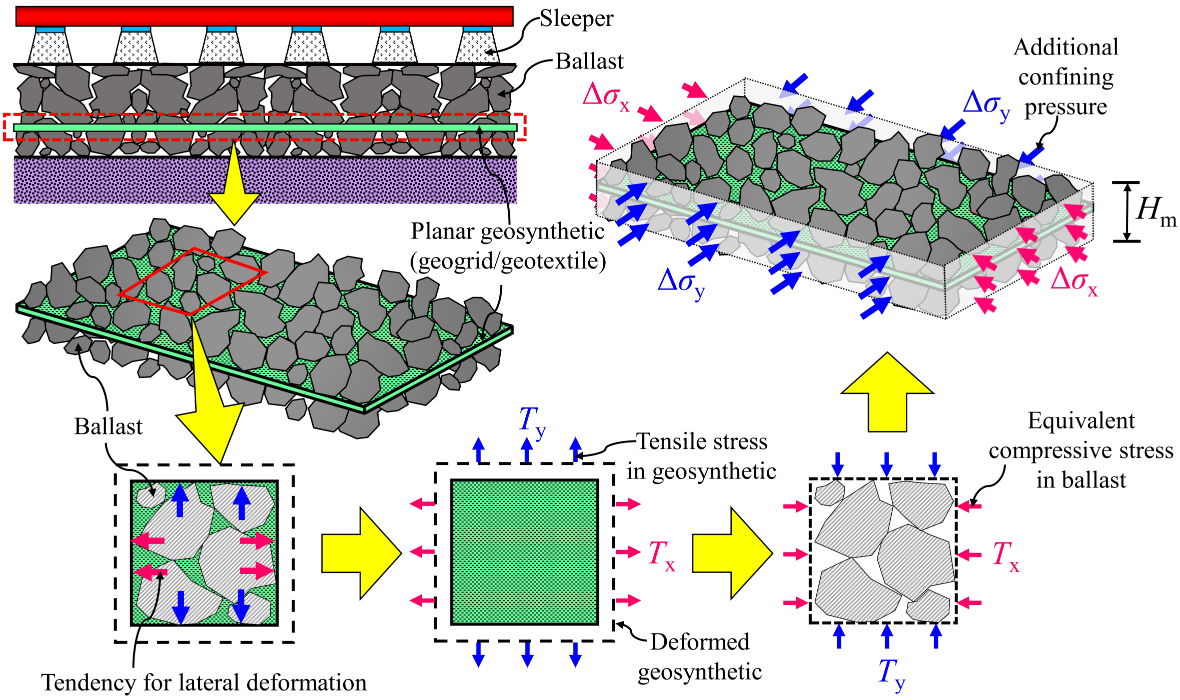

(a)

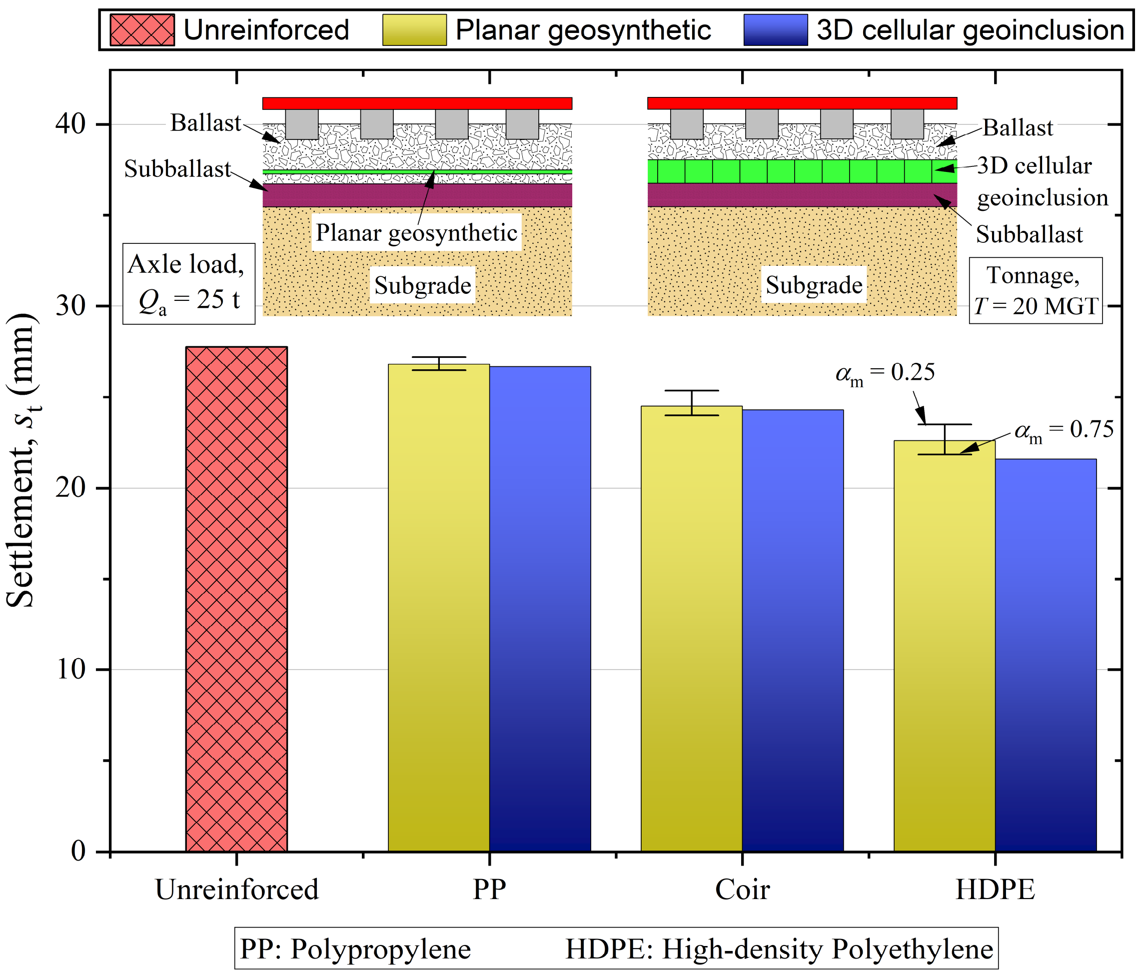

(b)

Figure 11. (a) Equivalence of stresses in planar geosynthetic to additional confining pressure in soil; **(b)** comparison of settlement accumulated in the unreinforced track and track reinforced using planar and 3D geosynthetics.

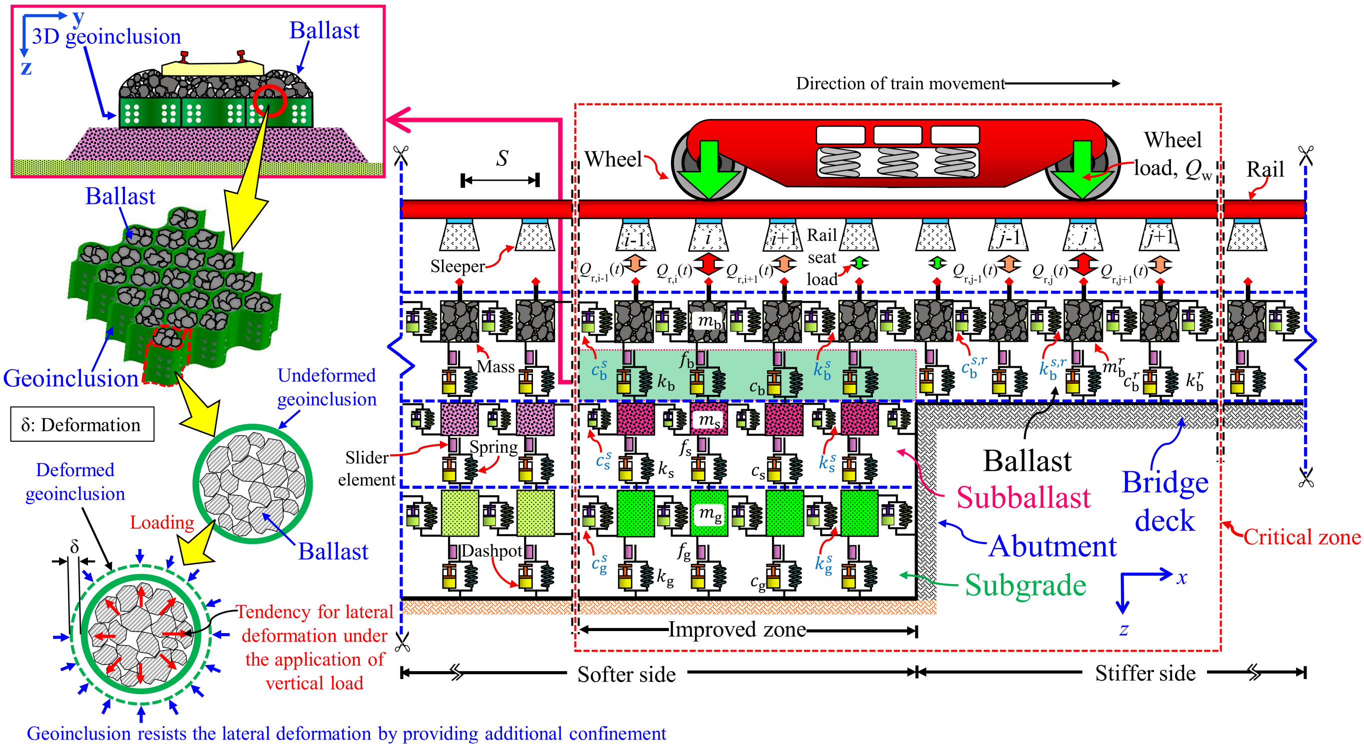

Figure 12. Geotechnical rheological model of a typical open track-bridge transition with 3D cellular geosynthetic reinforcement.

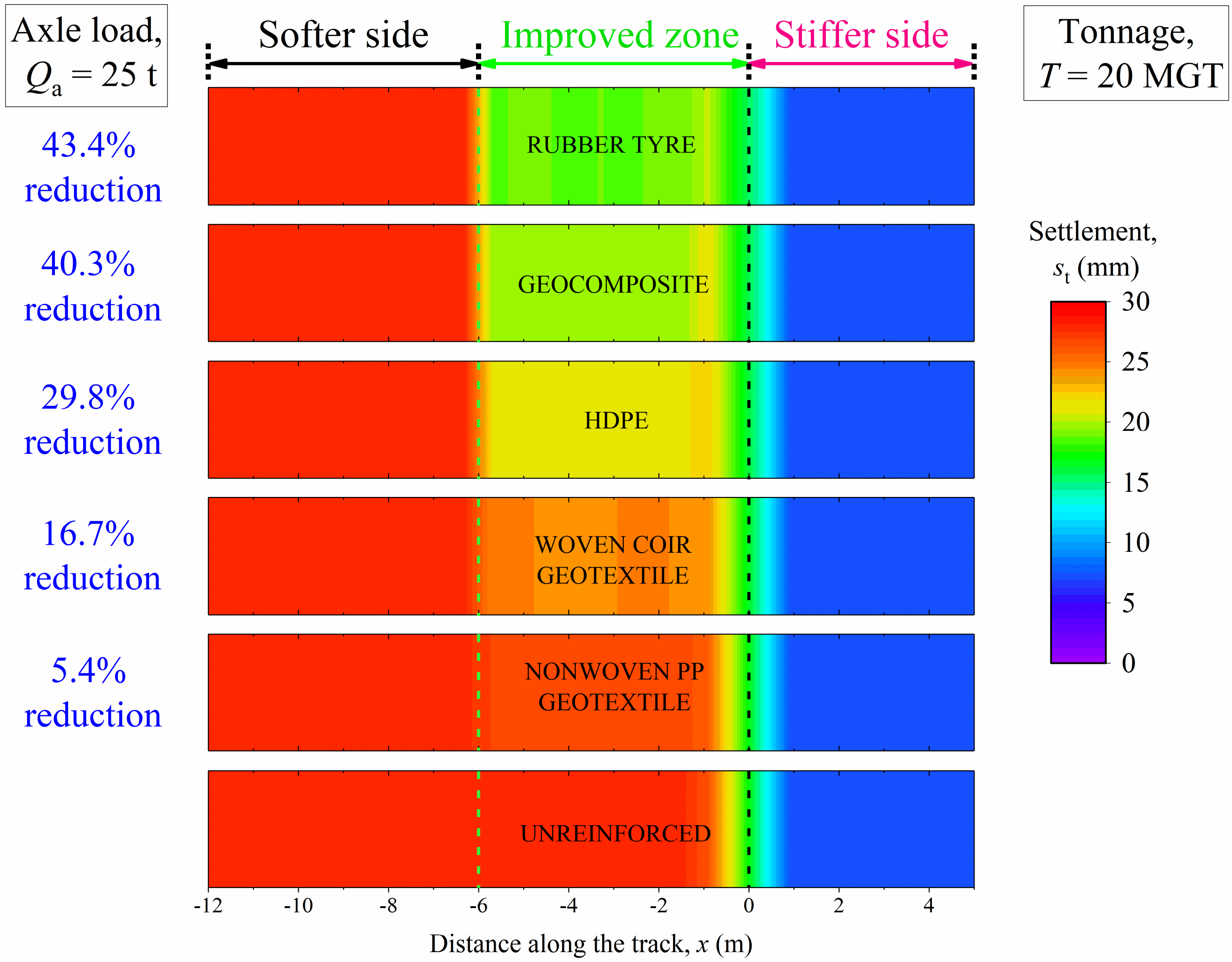

Figure 13. Variation of settlement along the length for unreinforced and reinforced track.

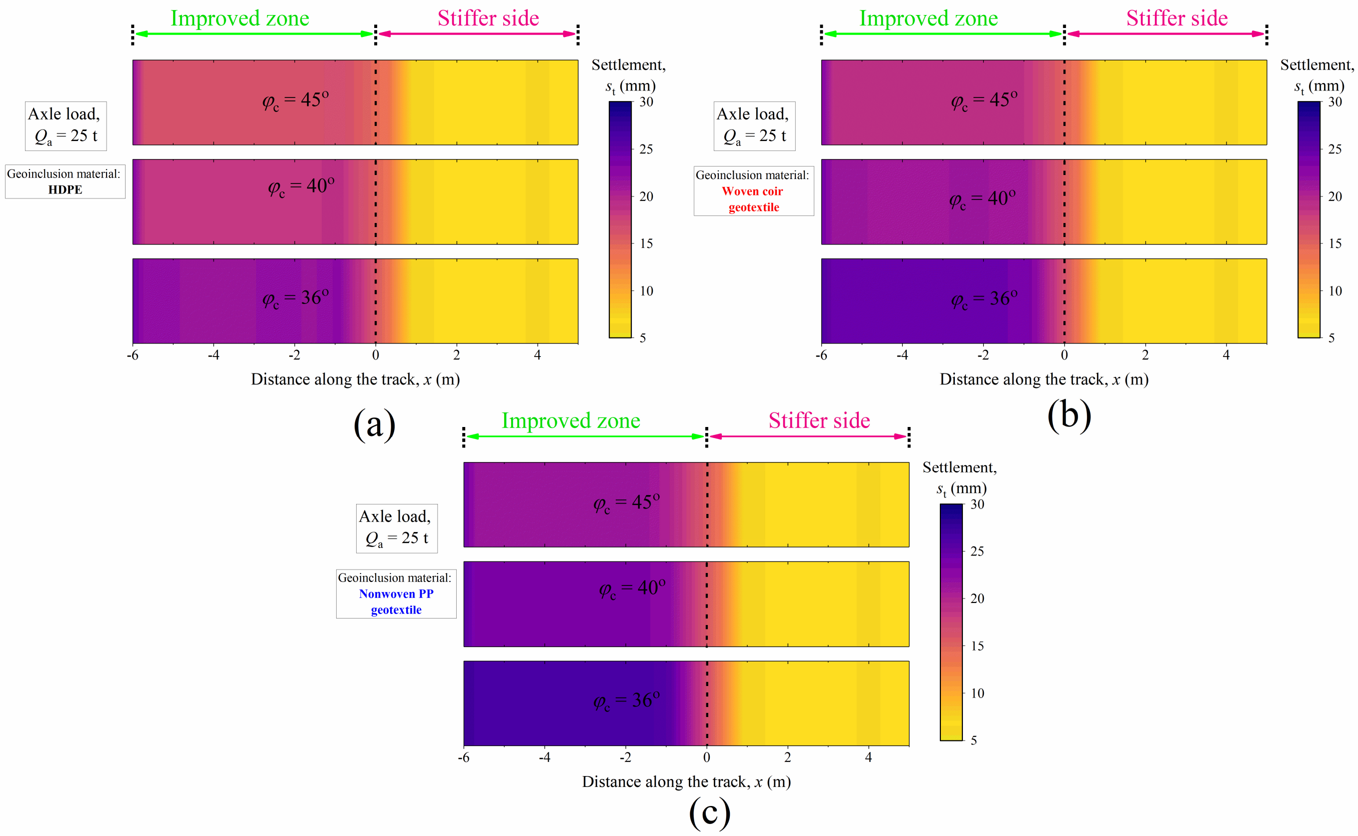

Figure 14. Influence of subgrade strength on effectiveness of artificial inclusions manufactured using: **(a)** HDPE; **(b)** woven coir geotextile; **(c)** nonwoven PP geotextile.

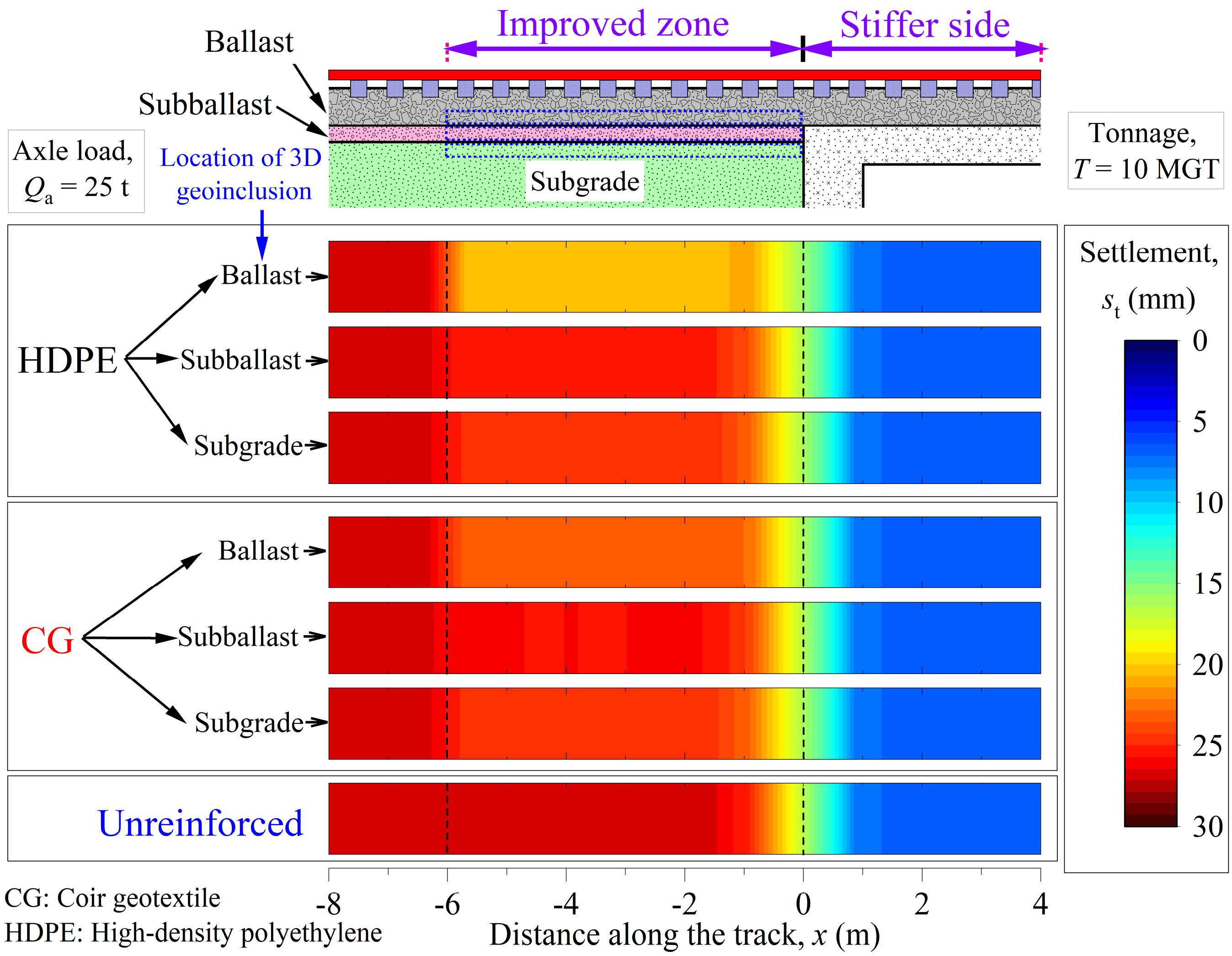

Figure 15. Variation of settlement along the length when 3D cellular inclusion is provided at different positions within the track.

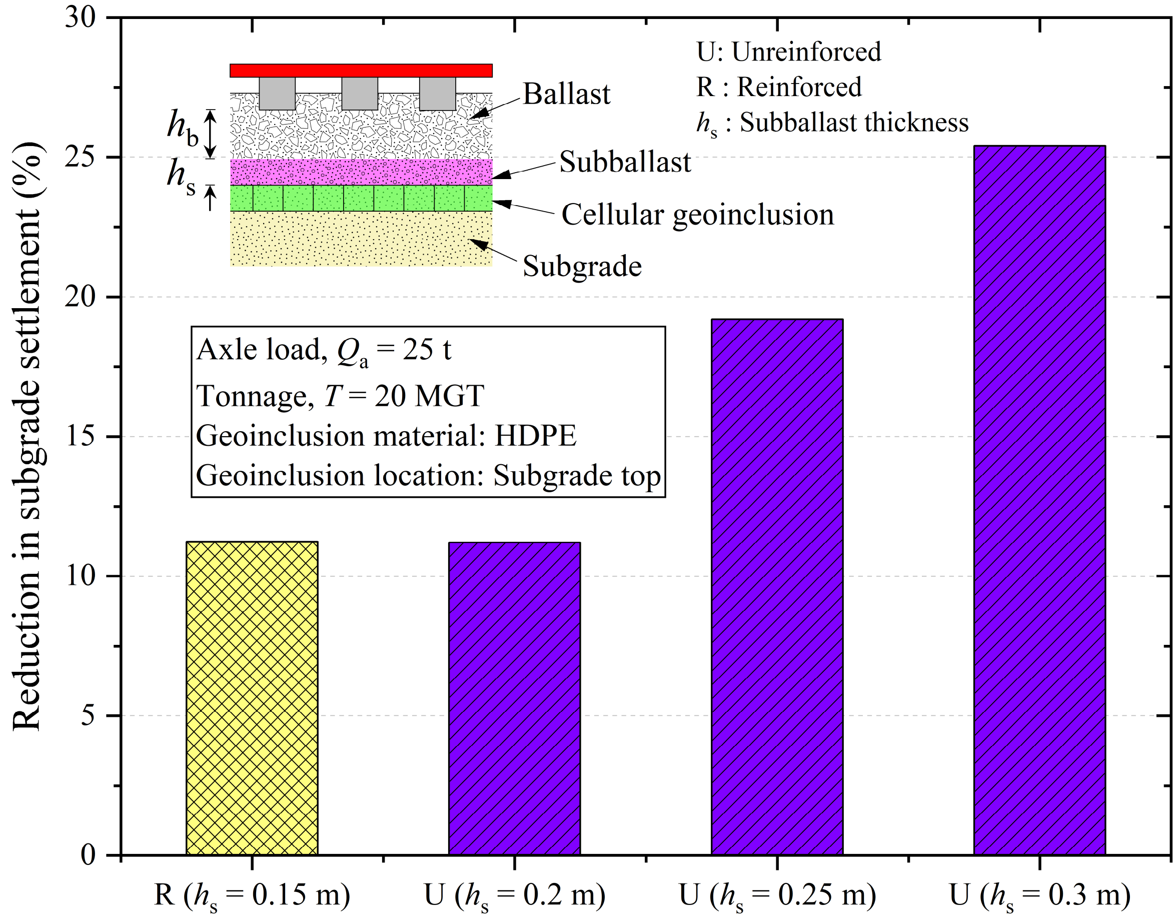

Figure 16. Reduction in subgrade settlement when cellular geoinclusion is provided at the top of the subgrade and when subballast thickness is increased from 0.15 m to 0.3 m.

Highlights

- Novel method to assess the adequacy of geoinclusions in improving track performance
- Combination of additional confinement and geotechnical rheological track models
- Method may assist railway engineers in deriving maximum benefits from geoinclusions
- Cellular inclusions reduce differential settlement at open track-bridge transition
- 3D inclusions made up of stiff materials reduced differential settlement by 30–43 %